Characterizing the transition from balanced to unbalanced motions in the southern California Current

Teresa K. Chereskin[1], Cesar B. Rocha[1,2], Sarah T. Gille[1], Dimitris Menemenlis[3], and Marcello Passaro[4]

[1]Scripps Institution of Oceanography, University of California San Diego, La Jolla, CA, USA.

[2]now at Woods Hole Oceanographic Institution, Woods Hole, MA, USA.

[3]Earth Sciences Division, Jet Propulsion Laboratory, California Institute of Technology, Pasadena, CA, USA.

[4]Deutsches Geodätisches Forschungsinstitut der Technischen Universität München, Munich, Germany

Key Points:

- At scales between 10 and 200 km, upper-ocean kinetic energy spectra follow a -2 power law.
- Observed transition scale from primarily balanced (geostrophic) to unbalanced motions is ~70 km.
- Seasonality is weak in spectra estimated from ADCP and altimetry observations.

Corresponding author: T. K. Chereskin, `tchereskin@ucsd.edu`

Abstract

As observations and models improve their resolution of oceanic motions at ever finer horizontal scales, interest has grown in characterizing the transition from the geostrophically-balanced flows that dominate at large scales to submesoscale turbulence and waves that dominate at small scales. In this study we examine the mesoscale-to-submesoscale (100 km to 10 km) transition in an eastern boundary current, the southern California Current System (CCS), using repeated ADCP transects, sea surface height (SSH) from high-resolution nadir altimetry and output from a 1/48° global model simulation. In the CCS, the submesoscale is as energetic as in western boundary current (WBC) regions, but the mesoscale is much weaker, and as a result the transition lacks the change in kinetic energy (KE) spectral slope observed for WBCs. Helmholtz and vortex-wave decompositions of the KE spectra are used to identify balanced and unbalanced contributions. At horizontal scales greater than 70 km, we find that observed KE is dominated by balanced geostrophic motions. At scales from 40 km to 10 km, unbalanced contributions such as inertia-gravity waves contribute as much as balanced motions. The model KE transition occurs at longer scales, around 125 km. The altimeter spectra are consistent with ADCP/model spectra at scales longer than 70/125 km, respectively. Observed seasonality is weak. Taken together, our results suggest that geostrophic velocities can be diagnosed from SSH on scales larger than about 70 km in the southern CCS.

1 Introduction

The partition between geostrophically balanced and unbalanced submesoscale upper-ocean flows and their projection on sea surface height (SSH) have practical implications for the interpretation of new altimeter missions that will resolve these relatively unobserved scales. A case in point is the upcoming launch of the Surface Water and Ocean Topography (SWOT) altimeter, which will provide SSH estimates with 10-15 km resolution [*Fu and Ubelmann*, 2014]. Theoretical predictions of submesoscale variability originally hypothesized largely geostrophic motions on scales smaller than 50 to 60 km in most parts of the ocean [e.g., *Lapeyre and Klein*, 2006; *Capet et al.*, 2008; *Le Traon et al.*, 2008]. Recent studies, however, suggest that when tides and inertia-gravity waves are resolved, submesoscale SSH has a signature of internal waves rather than geostrophic motions at these smaller scales [e.g., *Callies and Ferrari*, 2013; *Bühler et al.*, 2014; *Rocha et al.*, 2016a,b]. The above studies were primarily focused on strong-current systems. Here we examine the partition between geostrophically balanced and unbalanced submesoscale upper-ocean flows in a contrasting eastern boundary current region, the southern California Current System (CCS). The CCS is also of interest as the region chosen for the calibration/validation of the SWOT altimeter.

Studies of strong baroclinic jets, such as western boundary currents (e.g., the Gulf Stream and the Kuroshio) and the Antarctic Circumpolar Current (ACC), have identified a transition from balanced to unbalanced flow that occurs where the kinetic energy (KE) spectral slope flattens within the submesoscale range (100-10 km) [e.g., *Callies and Ferrari*, 2013; *Rocha et al.*, 2016a,b; *Qiu et al.*, 2017]. The wavenumber of the transition varies between current systems, but it occurs where the contribution from ageostrophic flows, such as inertia-gravity waves, outweighs that from geostrophically-balanced motions. For example, the transition occurs around 15 km in the Kuroshio [*Qiu et al.*, 2017], 20 km in the Gulf Stream [*Callies and Ferrari*, 2013] and around 40 km in the ACC [*Rocha et al.*, 2016a]. While the studies of these jets suggest a clear transition with a change in spectral slope around 15-40 km, *Qiu et al.* [2017] analyzed observations over a large range of latitudes in the northwest Pacific and found that the transition scale depended strongly on the local mesoscale variability, with longer scales corresponding to lower mesoscale energy level. Spectral slopes and slope changes have also been observed to vary more in regions outside of strong jets, and these characteristics have been used to infer differing dynamics [*Callies and Ferrari*, 2013; *Qiu et al.*, 2017]. Regions sampled with sufficiently high spatial resolution to examine the submesoscale are rare, but the southern CCS is one such region, because of the cruises by the California Cooperative Oceanic Fisheries Investigations (CalCOFI). The region is characterized by mesoscale (300-100 km) variability that is weak and submesoscale (100-10 km) variability that is as energetic as in the strong jets. This study combines high-resolution observations and numerical model output in order to examine the structure of the transition from geostrophically balanced to unbalanced motions in the southern CCS, at scales from 100 to 10 km, hereinafter referred to as the submesoscale transition. Although submesoscale dynamics extend to smaller length scales, this study is limited by the 10 km resolution of the CalCOFI observations.

2 Inferring dynamics from horizontal wavenumber spectra

Geostrophic turbulence theory has been used as a framework for analyzing high-frequency and high-wavenumber variability in the ocean. Isotropic interior quasi-geostrophic

(QG) turbulence theory predicts horizontal wavenumber (k) spectra of KE that rolloff as k^{-3} in the meso- to submeso- scale range [*Charney*, 1971] and SSH spectra that are expected to be two orders of magnitude steeper (k^{-5}). In contrast, surface QG (SQG) turbulence predicts a shallower $k^{-5/3}$ spectrum for KE [*Blumen*, 1978] and $k^{-11/3}$ for SSH. The theoretical predictions are made for two-dimensional isotropic spectra, but observations are more often made along a one-dimensional track. *Callies and Ferrari* [2013] summarize the theoretical predictions for isotropic two-dimensional wavenumber spectra and relate them to their one-dimensional along-track counterparts. Two key diagnostics emerge: the spectral slope and the ratio of across- to along-track KE components. *Callies and Ferrari* [2013] note that for an isotropic two-dimensional spectrum that follows a power law $k^{-n}, n > 0$, the one-dimensional spectrum will follow the same power law; furthermore, for a horizontally-nondivergent flow, the ratio of across- to along-track KE components of the one-dimensional KE spectrum should equal the power law exponent [*Charney*, 1971]. In other words, for a rolloff of k^{-n}, the across-track component should be n times more energetic than the along-track. Thus the ratio could be used as an indicator of geostrophic balance. *Bühler et al.* [2014] note that for the other extreme, i.e., a purely divergent flow, the converse is true; the along-track component should be n times more energetic than the across-track component [*Charney*, 1971]. Exploiting these properties, *Bühler et al.* [2014] develop a Helmholtz decomposition method for separating the divergent and rotational components of one-dimensional along-track KE spectra.

KE spectra estimated from satellite data and global models roll off as k^{-2} and SSH spectra as k^{-4}, and this has been interpreted as evidence for SQG turbulence [e.g., *Le Traon et al.*, 2008; *Lapeyre*, 2009; *Sasaki and Klein*, 2012]. KE spectra estimated from Gulf Stream velocity observations, however, roll off as k^{-3} in the 20-200 km range, with a ratio of across- to along-track KE of $\simeq 3$, and so both the slope and ratio are consistent with interior QG turbulence [*Wang et al.*, 2010; *Callies and Ferrari*, 2013; *Bühler et al.*, 2014]. Analyzing KE spectra from ACC velocity observations in Drake Passage, *Rocha et al.* [2016a] found k^{-3} KE spectral slopes in the 40-200 km range, similar to the Gulf Stream, but observed a flatter spectral slope in the 10-40 km range. Additionally, the KE component ratio in the ACC deviated significantly from the expectation of isotropic interior QG turbulence. Following the methodology of *Bühler et al.* [2014], *Rocha et al.* [2016a] showed that IGW likely accounted for the discrepancy between the observed spectra and the predictions of isotropic interior QG turbulence. *Qiu et al.* [2017] applied these methods to KE spectra estimated from repeated ADCP observations from 34°N to 3°N along 137°W and found that the transition scale lengthened in regions of weak mesoscale eddy energy.

In this study, we employ the same methods in order to extend the results to a different dynamical regime, an eastern boundary current system. As in prior studies, two diagnostics are used to interpret spectra in the context of geostrophic turbulence theory: the spectral slope of one-dimensional along-track wavenumber spectra and the ratio of across- to along-track KE spectra. Following *Bühler et al.* [2014] and *Rocha et al.* [2016a], a Helmholtz decomposition is employed to separate the rotational and divergent KE components, and a vortex-wave decomposition is used to further diagnose the flow into geostrophic and IGW components. We follow the steps outlined by *Rocha et al.* [2016a, Appendix C] for these two decompositions. The Helmholtz decomposition requires solving a coupled pair of ordinary differential equations in spectral space, under the assumptions that the rotational and divergent components are horizontally homogeneous, isotropic and statistically uncorrelated [*Bühler et al.*, 2014]. These are strong assumptions. In the California Curent region, there is some observational support for horizontal isotropy and homogeneity (Section 3.1). Results from the Helmholtz decomposition are more robust than the vortex-wave decomposition in that most of the assumptions are reasonable for the region, with the important caveat that the rotational and divergent components are not likely to be totally independent. The Helmholtz decomposition achieves an approximate separation into balanced and unbalanced motions corresponding roughly to the rotational and divergent components, respectively. The wave-vortex decomposition provides a more exact separation into vortex (balanced) and wave (unbalanced) components, but the tradeoff is that it requires the additional assumptions that the internal waves for the region can be characterized by the Garrett Munk [GM; *Garrett and Munk*, 1972] internal wave spectrum and that all divergent flow is due to internal waves. The GM spectrum is a composite from many observations and difficult to assess against any single set of observations. *Savage et al.* [2017] examined frequency-wavenumber spectra from seven regions in the same global numerical simulation used in this study. Although none of their regions overlapped with the southern CCS, in all seven regions they found good agreement with the GM spectral slope prediction of k^{-2} for tidal frequencies but flatter spectral slopes (k^{-1}) at supertidal frequencies, consistent with a more energetic model internal wave field.

3 Data and methods

3.1 Velocity data

Since 1984 CalCOFI has conducted quarterly hydrographic surveys along 6 parallel lines oriented approximately perpendicular to the coast from San Diego to Point Conception. The lines (numbered from south to north: 93, 90, 87, 83, 80 and 77) are spaced 74 km apart and extend from within 15 km of the coast to about 700 km offshore (Fig. 1). For this study we use shipboard acoustic Doppler current profiler (ADCP) velocity observations collected on 39 cruises over an 11-year period, 1993-2004, updated from *Gay and Chereskin* [2009]. We chose to analyze this decade-long interval because the data quality is high, and the data collection is the most consistent. Roughly half the cruises were carried out on the R/V New Horizon and the other half on the R/V David Starr Jordan; one cruise used the R/V Roger Revelle. In all cases, an RD Instruments 153.6 kHz narrowband ADCP was configured to sample with an 8-m pulse and an 8-m vertical bin. Sampling interval (1-,3-,5-min averages), transducer depth (4-5 m), and “blank-before-transmit” (4-12 m) varied between ships and cruises. ADCP data collection continues to the present on CalCOFI cruises, but the quality is uneven, with more gaps in the time series and more frequent changes in ships, instruments and ADCP configurations than in the record analyzed here.

The data were processed using methods and software developed at the University of Hawaii and described by *Firing and Hummon* [2010]. The main steps are summarized below. The constant sound speed used by the acquisition software is corrected to in situ sound speed calculated from temperature measured at the transducer and salinity appropriate for the CalCOFI region (33 psu). The velocities are navigated from ship-relative to absolute ocean currents using Global Positioning System (GPS) position measurements to estimate ship speed. Smoothed positions and ship speeds are calculated by filtering a depth-averaged layer of absolute ocean current with a Blackman filter (900-s half-width) and then subtracting out the ship-relative current. Since the filter is tapered, ship speed estimates separated by 900 s are approximately independent. An overall amplitude and misalignment angle (correcting for a mean gyrocompass-transducer misalignment) are estimated and applied. The data were edited, primarily to remove data at the end of the profile contaminated by bottom interference in the Southern California Bight region where there is complex and shallow topography within range of the ADCP. In order to create a uniform time series, the ocean currents from each cruise were block-averaged over 900-s intervals (about 5-km along-track at a steaming speed of 5 m s^{-1}) and interpolated to fifty 8-m depth bins, from 16 m to 408 m.

ADCP instrumental bias was minimized through selection of profiling parameters affecting signal tracking [*Chereskin and Harding*, 1993; *Chereskin and Trunnell*, 1996]. Instrumental errors in ship-relative currents are quite small, less than 0.5 cm s^{-1} for a 900-s average. GPS quality varies over the time series. During the 1990s, the Department of Defense intentionally degraded GPS positions (SA or selective availability). However, military grade receivers (P-code) that were not affected by SA came into use on research vessels. Between 1995 and 2004, P-code quality GPS was available on 31 of the cruises; the remaining 8 were affected by SA. The uncertainty in absolute current due to errors in ship position over a 900-s average is estimated to be 4 cm s^{-1} (spectral noise level of 0.0015 m^2s^{-2}/cpkm) in the case of SA GPS measurements and less than 1 cm s^{-1} (spectral noise level of 0.0001 m^2s^{-2}/cpkm) in the case of P-code measurements [*Chereskin and Harris*, 1997]. ADCP KE estimates lie above these noise levels.

For this study we present ADCP spectra calculated along CalCOFI line 90. Line 90 is one of the longest lines and has the additional advantage that KE spectral estimates from high frequency radar (HFR) are available at the inshore edge [*Kim et al.*, 2011]. We used 650-km length segments, rotated by 30 degrees counterclockwise onto an along/across track coordinate system, averaged to a uniform 5-km spacing, with gaps less than 25 km filled by linear interpolation. A gridded time-mean velocity section is not removed; KE spectra calculated after removing a mean are indistinguishable from the ones shown here. For each transect, at each depth, the velocity is rotated into along and across track components, detrended, multiplied by a Hanning window and Fourier transformed. Spectral estimates are calculated by multiplying the Fourier coefficients by their complex conjugate and averaging over all realizations in each of 15 depth layers. Two-bin depth averaging is used between 16 and 152 m; four-bin depth averaging is used between 160 and 296 m. Confidence limits are calculated assuming that the Fourier coefficients are normally distributed and their magnitudes squared are chi-square distributed [*Bendat and Piersol*, 2010]. Each transect is assumed independent; in depth averaging, every other depth bin is assumed independent. Data gaps increase with depth, resulting in fewer estimates at deeper levels. Increasing the vertical averaging from two to four depth bins keeps the confidence limits approximately constant for all layers. ADCP spectra estimated for the other lines (not shown) are similar to line 90, which suggests that the assumption of horizontal homogeneity is reasonable for the CalCOFI region. Observational support for horizontal isotropy comes from velocity variance ellipses that are nearly circular (not shown). We average together spectra from multiple CalCOFI lines in order to increase the confidence in seasonal estimates (Section 4.3). Treatment of the other lines is the same as that described for line 90. For multi-line spectral averages, we used a maximum length segment of 340 km (length of line 77) with origin at the offshore end of each of the lines (Fig. 1).

Our interpretation of the ADCP KE spectra makes the same fast-tow assumption used by previous authors, i.e., that the ship speed is faster than the propagation speed of the fluctuations [*Callies and Ferrari*, 2013; *Rocha et al.*, 2016a; *Qiu et al.*, 2017]. At a steaming speed of 5 m s^{-1}, the ship travels 10 km in about 30 mins and 100 km in about 5.5 hours. The fast-tow assumption is reasonable for high-frequency internal waves that project onto small horizontal scales and for large-scale geostrophic eddies that generally have time scales much longer than a day. Fluctuations with intermediate scales such as tides and near-inertial currents will be aliased. In the model the mesoscale flow is coherent over the line 90 sampling period (48 hours); Hovmöller diagrams (not shown) suggest that there is some propagation of high-frequency signals along line 90, likely internal tides. The effect of the aliasing on the spectra is difficult to assess, however, hence the importance of comparing with other observations such the HFR, altimetry and the numerical simulation, where the sampling is truly fast-tow. An additional complication for CalCOFI cruises is that the ship stops for hydrographic sampling, with stations spaced roughly every 70 km and lasting about 2-2.5 hours. For wavelengths shorter than 70 km, we examined the effect of the stations by computing KE spectra for underway-only segments and compared to spectra computed from the gridded data (not shown). The stations do not significantly alter the spectral slopes nor the KE component ratios.

3.2 Altimetry data

As an independent measure of high-wavenumber variability, we compute spectra from altimetric sea surface height for a selection of exact repeat altimeter tracks that are roughly perpendicular to the California coast, as shown in Fig. 2, and are in the same region as the CalCOFI sampling lines of the ADCP, although they are more meridional.

Standard altimeter products typically have a 7–15-km footprint [e.g., *Dibarboure et al.*, 2014] and report data at 1 Hz, roughly equivalent to 1 sample every 6-10 km. Given the autocorrelation of sea surface height, the effective spatial resolution of 1-Hz analyses of along-track altimeter data have emphasized resolving features at scales larger than 30-60 km [e.g., *Stammer*, 1997; *Chelton and Schlax*, 2003]. Since this study is focused on high-wavenumber processes, we examine three altimeter products, each selected because of its potential to provide high-wavenumber information: a retracked version of Jason-1/2 data and data from two satellites that have introduced newer technology intended to resolve higher-wavenumber processes: AltiKa and Sentinel-3.

For the Jason-1 and Jason-2 Ku-band altimeters, we use data processed with the Adaptive Leading Edge Subwaveform (ALES) algorithm [*Passaro et al.*, 2014], which was developed to meet the requirements of small-scale coastal oceanography, while providing a consistent product for the open ocean. Radar altimeters typically exhibit a "spectral bump" at high wavenumbers that has been attributed to preferential satellite returns from "bright" spots within the satellite footprint, associated with rain or backscatter coefficient (σ_0) "blooms" [e.g., *Dibarboure et al.*, 2014; *Raynal et al.*, 2018]. The ALES retracking procedure considers only a portion of the radar signal, with focus on the leading edge, and therefore partially avoids the inhomogeneities in the backscatter strength. This should reduce the effect of the spectral bump compared to the standard processing as shown by *Smith et al.* [2017]. Jason-1 launched in December 2001, and data are available from January 2002 through January 2009. Jason-2 launched in June 2007, and data are available from July 2008 through August 2016. Together this provides a potential of 557 cycles, of which we use 80 to 90%, eliminating all satellite passes with significant noise that could be associated with waves, rain contamination, or satellite anomalies. The Jason satellites return to each ground track every 9.9 days, providing one track of nadir data each cycle. We use three groundtracks, identified in the ALES product as 43, 119, and 195. All environmental corrections are applied (including tides), and the mean sea surface is removed. The sea state bias correction is recomputed using ALES estimations of significant wave height and wind at high frequency, as explained by *Passaro et al.* [2018]. Data are screened to remove measurements when significant wave height is reported to be greater than 11 m, when the radar fitting coefficient ('Err') is greater than 0.3, when the sea surface height anomaly exceeds 0.7 m, or when $\sigma_0 > 30$ dB.

The AltiKa altimeter launched in February 2013 as a joint French-Indian project with a sun-synchronous orbit that followed the ground track previously used by the European Space Agency altimeters, ERS and Envisat, with a 35-day repeat [*Verron et al.*, 2015]. The use of the Ka band allows a reduced footprint and higher pulse-repetition frequency, which leads to higher precision in the range estimation at 40 Hz, even when compared to the 20-Hz sampling of the classic Ku-band altimeters [*Quartly and Passaro*, 2015; *Verron et al.*, 2015]. We used AltiKa in earlier work [*Rocha et al.*, 2016a], and the processing and quality control followed the same editing criteria [*Durand et al.*, 2008; *Roblou et al.*, 2011; *Birol et al.*, 2010; *Rocha et al.*, 2016a]. AltiKa returned data on a consistent groundtrack from approximately October 2013 until May 2016. For the California Current, we use a total of 9 groundtracks, from the 25 cycles during this period, yielding 208 usable passes after quality control. AltiKa environmental corrections, including tides, are provided at 1 Hz and, for this analysis, we use a spline interpolation to obtain environmental corrections at 40 Hz. The 1-Hz sampling of the corrections effectively limits their influence to scales longer than 15–20 km. For smaller scales, the spectral energy of the spline-interpolated corrections drops off rapidly; this rapid drop off would only pose a problem if the corrections themselves were highly energetic at 1 Hz, in which case, the spectral drop-off could lead to an unphysical drop in spectral energy for scales around 15–20 km.

The Sentinel-3 altimeter (red lines in Fig. 2) uses delayed Doppler (or synthetic aperture radar) processing [*Raney*, 1998; *EUMETSAT*, 2017], which is designed to achieve significantly higher signal-to-noise ratios [*Heslop et al.*, 2017]. However, Sentinel-3's sun-synchronous orbit, with a 27-day repeat, is distinct from that of previous altimeters (compare red and orange lines in Fig. 2), so the mean sea surface height is not well characterized along its ground tracks, and there are still comparatively few satellite passes over each of the Sentinel-3 ground tracks in the California Current, meaning that sea surface height anomalies from Sentinel-3 may have more residual geoid contamination than those from other satellites. Previous studies based on Cryosat-2 (also a delay-Doppler altimeter) in the Indonesian seas suggest that the use of a global mean sea surface model to remove the mean sea surface height along sparsely sampled ground tracks does not amplify the overall spatial variance of SSH within 50 km × 50 km test patches [*Passaro et al.*, 2016]. Here, however, we are interested in along-track data and high-wavenumber spectra, and therefore we cannot exclude the possibility of residual geoid contamination in the along-track means. In total, we use 7 ground tracks from 20 cycles of data from the time period between January 2017 and May 2018, yielding 110 usable passes after quality control. Data are used only in regions deeper than 2000 m depth, because geoid uncertainties are expected to be larger in shallow water. For this analysis, we use sea surface height anomalies (ssha) computed relative to the Earth's mean sea surface, with environmental corrections, including a tidal correction, applied. The typical standard deviation of the reported ssha is about 6 cm; large standard deviations are indicative of questionable satellite passes. For this analysis satellite passes with along-track ssha standard deviations exceeding 11 cm are not used. Satellite passes are also not used if, after demeaning, they have a standard deviation greater than 10 cm.

For all three altimeter data streams, sea surface height data are processed to retain high-wavenumber structure, while removing the background time-mean field, which could be associated with stationary geophysical structures that determine the geoid. The time-mean signal measured by the altimeter is associated with the Earth's geoid, so we remove the time-averaged sea surface height to focus on the oceanographic portion of the signal. Our processing procedure takes into account the fact that the latitude and longitude coordinates reported in the data files shift slightly each cycle. High-frequency 20-Hz altimeter data are first linearly interpolated to a common reference track. Then sea surface heights on the reference track are time-averaged to produce a mean sea surface height. One possible strategy would be to demean and analyze the interpolated sea surface heights. However, we do not do this, since linear interpolation acts as a 2-point smoothing process, which effectively applies a filter to the high-wavenumber spectrum. Instead, for each cycle the along-track mean sea surface height is linearly interpolated onto the cycle-specific latitude/longitude points to produce the mean most appropriate for the individual cycle. Data are then demeaned, Hanning windowed in the same way as the velocity records, Fourier transformed and averaged together to produce spectra. In the case of Jason 1 and Jason 2, we compute separate mean sea surfaces for the two satellites. Final spectra combine records from the two satellites.

3.3 LLC numerical simulation

We use output from a 1/48° numerical simulation that is a forward solution of the Massachusetts Institute of Technology general circulation model [MITgcm; *Marshall et al.*, 1997; *Hill et al.*, 2007] configured on the Latitude-Longitude Cap (LLC) grid [*Forget* *et al.*, 2015]. The model was spun up through a hierarchy of runs with increasing horizontal resolution, all with 90 vertical levels. The initial conditions are from a 1/6° adjoint-method-based state estimate constrained with millions of observations spanning 2009–2011 [*Menemenlis et al.*, 2008] and provided by the Estimating the Circulation and Climate of the Oceans (ECCO) project. The 1/48° simulation, (LLC 4320, nominal grid spacing of about 2 km in the CCS region, effective resolution of about 8 km), is forced by the 16 most-significant tidal components and 6-hourly surface atmospheric fields from the 0.14° European Centre for Medium-Range Weather Forecast (ECMWF) analysis starting in 2011. The LLC 4320 simulation is the same one analyzed by *Rocha et al.* [2016b] and *Qiu et al.* [2018]. The tidal forcing is a critical aspect of the numerical simulation, as significant IGW energy results from the conversion of barotropic tidal energy due to interaction with topography. We compute KE and SSH variance spectra from snapshots of hourly-averaged LLC 4320 model output along a line 90 transect in the simulation (Fig. 3). Spectra are also computed from daily averages in order to see the effect of filtering the tides and high frequency IGW. The spectra are computed as described for the velocity and SSH observations. Additionally, the one-year run of the LLC 4320 is used to examine seasonal variability. As in *Rocha et al.* [2016b] we compute the second-order statistics of vertical vorticity,

$$\zeta = v_x - u_y, \tag{1}$$

lateral rate of strain,

$$\alpha = [(u_x - v_y)^2 + (u_y + v_x)^2]^{1/2}, \tag{2}$$

and horizontal divergence,

$$\delta = u_x + v_y, \tag{3}$$

where u and v are, respectively, the zonal and meridional velocity components. These higher-order statistics estimated over the subdomain shown in Fig. 3 emphasize fine lateral scales and are used to grossly differentiate between submesoscale turbulence and IGW. The separation is approximate, however, as IGW have vorticity and small-scale eddies are divergent.

We also computed the meridional component of geostrophic velocity v_g along a line of constant latitude (32°N) and the zonal component of geostrophic velocity u_g along a line of constant longitude (122°W) in the subdomain shown in Fig. 3 using the geostrophic relation:

$$(u_g, v_g) = \frac{g}{f}(-\eta_y, \eta_x), \tag{4}$$

where g is gravity, f is the Coriolis parameter and η is the model sea surface height. Centered differences of η (nominally 4 km separation) produced estimates that were co-located with model velocity estimates.

4 Kinetic energy spectra

4.1 Partition between balanced and unbalanced motions

Line 90 KE spectra estimated from the ADCP observations and from the LLC 4320 hourly-averaged currents at 20 m depth have similar shape and energy levels; the total surface KE spectrum from HFR estimates [pers. comm. S.-Y. Kim, *Kim et al.*, 2011] agrees well with the ADCP and model spectra (Fig. 4). Although the spectral slope is not constant through the submesoscale wavenumber range, it is closer to -2 than -3. Computing daily-averaged currents in the model effectively removes the tides and higher frequency components and reduces KE at all spatial scales, especially short ones. The slope of the model-daily KE spectrum is steeper (closer to -3) than the model-hourly spectrum (Fig. 4).

KE components are defined as one half of the across-track and along-track velocity variance spectra, respectively, such that their sum is the total KE spectrum. Slopes of the KE components for the ADCP and the model-hourly spectra are similar to their respective total KE spectrum for the submesoscale range (Figs. 5 and 6, upper left). The ratios of the across-track to along-track components, however, are not constant for the ADCP and the model-hourly KE estimates. For the ADCP, the ratio is about 1.8 for wavelengths L in the range $70 < L < 300$ km, and it is about 1 for $L < 40$ km (Fig. 5 upper left). For the model-hourly KE estimates, there is a switch in dominant KE component: the across-track component dominates for wavelengths $125 < L < 300$ km, the components are about equal for $30 < L < 125$ km, and the along-track component dominates for $L < 30$ km (Fig. 6 upper left). The switch in dominance at high wavenumbers, while not significant at 95% confidence, persists over the high end range, $7 < L < 30$ km. For the model-daily components, the ratio of the across- to along-track components is fairly consistent, averaging about 2.6 with a standard deviation of 0.4 over wavelengths $10 < L < 100$ km

(Fig. 6 upper left). The model-daily spectra are consistent with balanced, nondivergent geostrophic motions.

Decomposing the line 90 ADCP KE spectra into rotational and divergent components [*Bühler et al.*, 2014; *Rocha et al.*, 2016a] indicates that the rotational component dominates for $L > 70$ km; KE is equipartitioned between rotational and divergent components for $L < 40$ km (Fig. 5, upper right). Following *Bühler et al.* [2014] and *Rocha et al.* [2016a], we diagnose the wave and vortex components from the Helmholtz decomposition, assuming the Garrett Munk spectrum for the IGW component with stratification estimated from CalCOFI hydrography [*Bograd et al.*, 2001]. Specifically, we assume that the ratio of rotational to divergent wave energy in the California Current region is the same as in the GM model. The vortex components are purely rotational. The slopes are about -2 over most of the wavenumber range, and the ratio between KE components is approximately constant, with the across-track component about twice as large as the along-track component (Fig. 5, lower left). These characteristics are consistent with geostrophic motions. The wave components can have both a rotational and a divergent part. The amplitude of the wave contribution is quite small at long wavelengths, but it contributes about equally to the total KE spectrum at wavelengths shorter than 40 km (Fig. 5, lower right). At wavelengths shorter than about 25 km, the two wave components have similar slopes, about -2, and the along-track exceeds the across-track component by about a factor of 2, consistent with purely divergent flow. The decompositions suggest that there is a change in dynamics that occurs at about 70 km wavelength, but without a change in slope, since the slopes of the wave and vortex components are both about -2, at least over the wavenumber ranges where they contribute significantly to the total KE. The energy level of the vortex and wave components are approximately equal over the interval $10 < L < 40$ km, consistent with the equipartion of the rotational and divergent KE and with wave KE that is mostly divergent.

Decomposing the model-hourly KE spectra in a similar manner, the rotational component dominates at the longest length scales, but the switch in dominance between rotational and divergent KE components occurs earlier than for the ADCP, near 125 km (Fig. 6, upper right). Equipartitioning between rotational and divergent components is seen from $50 < L < 125$ km. At shorter length scales, $L < 50$ km, the divergent component clearly dominates the KE (Fig. 6, upper right). Using the same Garrett Munk assumptions as for the ADCP, the vortex and wave components have slopes of about -2.2 and ratios of about 2 for the fitted submesoscale wavenumber range (Fig. 6, lower panels). Because the model vortex KE decreases abruptly at the transition around $L \simeq 125$ km, the spectral slope appears to change from about -3 to -2. The key differences between the model and ADCP spectra are found in the vortex-wave components; the model has less vortex and more wave energy than observed over the submesoscale. The daily-averaged model spectra have greatly reduced energy at high wavenumbers (Fig. 6, upper left) and therefore a reduced wave component in the decomposition (not shown); hence spectral slopes are steeper for the model-daily versus model-hourly spectra.

4.2 Depth dependence

The ADCP and LLC 4320 model KE spectra show similar depth dependence (Fig. 7). At the longest wavelengths resolved ($L > 200$ km) the spectra are self similar with depth; KE decays but the shape of the spectrum is maintained. The model has similar KE as observed at the longest scales resolved, but KE decays more slowly with depth in the model estimates than observed. At scales $100 < L < 200$ km, there is a compression of the spectral lines. Over the range $50 < L < 100$ km there is a split at around 100 m depth, with slightly elevated KE in the layers above and slightly depressed KE in the layers below. The compression of spectral lines is most pronounced at shorter wavelengths, $L < 25$ km, where deeper KE levels exceed those of slightly shallower ones. Although a slope of -2 for the shallowest KE spectrum is roughly consistent with SQG predictions of -5/2, the observed depth dependence is not. SQG turbulence predicts a steepening of spectral slope with depth, approaching the interior QG slope of -3 [*Blumen*, 1978]. In contrast, these slopes remain -2 or less (Fig. 7).

The decomposition into vortex-wave components for the ADCP spectra show that the compression is entirely in the wave component (Fig. 8, right). Vortex KE (Fig. 8, left) decays with depth. The compression in the wave component over these upper-ocean depths could be due to low vertical-mode internal waves (heaving); it also occurs in the model (not shown). The slope of ADCP vortex KE remains roughly -2 over the submesoscale for the depths examined. The slope of the wave KE changes more with wavenumber, flattening at longer wavelengths (Fig. 8). The ratio of the ADCP vortex:wave KE is used to look at the depth dependence of the transition scale (Fig. 9). Ratios larger than unity are interpreted as primarily balanced motions. The transition scale is the wavelength at which the ratio equals unity, with ratios less than unity interpreted as primarily ageostrophic motions. The curves fall into two groupings. Ratios at depths less than 100 m have transition scales $L \simeq 70$ km (52 m depth is anomalous in that it drops to a local minimum at 70 km but does not fall to unity). Ratios at depths greater than 100 m have transition scales $L \simeq 120$ km. The split in transition scales at 100 m depth occurs within the wavelenth range $50 < L < 100$ km where there is a also a split in KE, with elevated KE above and depressed KE below (Fig. 7).

4.3 Seasonality

The seasonality of submesoscale turbulence has been the focus of numerous recent studies [e.g., *Sasaki et al.*, 2014; *Qiu et al.*, 2014; *Brannigan et al.*, 2015; *Callies et al.*, 2015; *Thompson et al.*, 2016; *Buckingham et al.*, 2016; *Rocha et al.*, 2016b; *Qiu et al.*, 2018; *Su et al.*, 2018]. Using the same LLC 4320 simulation as used here, *Rocha et al.* [2016b] found evidence for seasonality in submesocale IGW as well as in submesoscale turbulence in the Kuroshio Extension region. The tidal forcing included in the LLC simulations distinguished *Rocha et al.* [2016b] from other modeling studies of the seasonality of submesoscale motions [*Sasaki et al.*, 2014; *Qiu et al.*, 2014] and allowed identification of the seasonal cycle of the IGW. They found that submesoscale turbulence peaks in winter/spring, whereas submesoscale IGW peak in summer/fall. Studies of the global LLC 4320 simulation found out-of-phase seasonality in surface balanced and unbalanced motions everywhere except the Pacific and Indian sectors of the Southern Ocean, where mixed layers remain deep even in summer [*Qiu et al.*, 2018; *Su et al.*, 2018].

Following *Shcherbina et al.* [2013] and *Rocha et al.* [2016b], we use higher order statistics of horizontal velocity gradient fields: root-mean-square (RMS) vertical vorticity, lateral rate of strain, and horizontal divergence, to examine more closely the seasonality in the LLC 4320 simulation in the CalCOFI region. We use the CalCOFI ADCP observations to groundtruth the model results.

Figure 10 shows monthly averages of RMS surface vorticity, strain and divergence computed over the model subdomain corresponding to the CalCOFI region (Fig. 3). The seasonality in the California Current region is similar to that observed in the Kuroshio Extension, with RMS vertical vorticity and lateral rates of strain peaking in March. Peak values of vorticity approach $0.23f$, where f is the local planetary vorticity, and are about $0.15f$ in summer (red solid line in Fig. 10). Strain peaks in March ($0.3f$) with a minimum in May ($0.24f$) but remains relatively low over the summer and fall months (blue solid line in Fig. 10). Although the phasing in the CCS is similar to the Kuroshio Extension, the maximum RMS amplitudes of the vorticity and the strain rate are about 40% of Kuroshio values.

The divergence estimated from model-hourly values is out of phase with the vorticity and strain fields, with a peak value of about $0.2f$ in October (green solid line in Fig. 10); this level lies between vorticity and strain levels which are both close to their seasonal minima in October. The phase and amplitude of the horizontal divergence is similar to that estimated for the Kuroshio region. Daily averaging effectively removes the tides and higher frequency IGW (dashed lines in Fig. 10). Monthly averaging of RMS divergence estimated from model-daily values greatly reduces the amplitude and reverses the phase, with the peak now occurring in winter (February), similar to the other RMS fields. Monthly averaging of RMS vorticity and strain from model-daily values reduces the amplitude but does not change the phase (dashed lines in Fig. 10). Our interpretation is the same as in *Rocha et al.* [2016b]; with the IGW component reduced, the seasonal cycle of vertical vorticity, lateral strain rate and horizontal divergence are in phase and are due to submesoscale turbulence. The submesoscale IGW are out of phase with the turbulence. The phase cancellation reduces the seasonal cycle of upper ocean submesoscale KE, and this is seen in model-hourly spectra which do not show significant seasonality in the model's contrasting seasons of spring and fall (left panel, Fig. 11). Seasonality is evident, however, in the model-daily spectra where daily averaging reduces the IGW energy; the seasonality is confined to depths shallower than 130 m (right panel, Fig. 11). Although not the focus of this study, seasonality is also evident in the mesoscale (L > 200 km), and the phase is reversed relative to the submesoscale, with mesoscale KE peaking in fall whereas submesoscale KE is largest in spring (Fig. 11).

Similar to the model results, KE spectra estimated from the ADCP data on line 90 do not reveal significant seasonality; however, the uncertainty in the seasonal estimates is quite large (Fig. 12 left). We can increase the statistical significance by treating the CalCOFI lines as independent estimates, to increase the confidence in the individual cruise estimates over that obtained from using line 90 alone. For these spectra, a common maximum section length of 340 km was used, decreasing the value of the largest wavelength resolved. Winter KE is significantly larger than the other seasons for wavelengths of 340 km to about 100 km (Fig. 12 right). At smaller scales there is no significant seasonality at

95% confidence. Decomposing the spectra into wave and vortex contributions reveals that winter vortex KE is significantly larger than summer vortex KE at almost every wavenumber (Fig. 13 left). At scales less than 70 km, summer wave KE is high, but except at a few wavenumbers, it is not statistically distinguishable from the other seasons (Fig. 13 right).

The model is sampled uniformly in time with sufficient temporal resolution to resolve the seasonal cycle. While the quarterly sampling of CalCOFI allows an attempt to assess seasonality, the sampling falls short of resolving the seasonal cycle. The cruises tend to repeat in fixed months: the winter cruise is normally in January/February, the spring cruise in March/April, the summer cruise in July and the fall cruise in September/October. In addition to concerns about the distribution of cruises, the number of cruises per season in this dataset is relatively small, about 9. A final concern is that the shallowest depth sampled is 16 m, which could miss a significant fraction of a seasonal IGW signal in summer and fall when the mixed layer over much of the CCS lies above that depth, although the model seasonal signal persists to about 130 m depth. More years of sampling with more temporal and vertical resolution closer to the surface, such as with repeated glider tracks, are needed to resolve the seasonal cycle from observations.

5 Sea surface height spectra

Satellite altimeter measurements of sea surface height provide an independent measure of wavenumber variability to compare with ADCP measurements. For geostrophic flows, velocity is computed from the first derivative of sea surface height: since spectral quantities are squared, this means that, in the geostrophic regime, the k^{-2} kinetic energy spectra found from ADCP velocities imply an expectation of k^{-4} spectral slopes for sea surface height [e.g., *Le Traon et al.*, 2008]. For unbalanced or ageostrophic flows (i.e., for $L \lesssim 70$ km, as identified from the ADCP data), there is not a similar simple spectral slope relationship between velocity and height spectra. Figure 14 shows spectra computed from altimetric sea surface heights and from the LLC 4320 model.

The Jason-1/2 spectra with ALES processing [*Passaro et al.*, 2014], shown in blue in Fig. 14, are red for low wavenumbers with slopes near k^{-4}, flatten to white for scales shorter than 20-30 km, are red between scales of 2-10 km, and then have a white noise floor at high wavenumbers, which is associated with instrumental white noise [*Dibarboure et al.*, 2014]. Despite their geographic separation, all 3 groundtracks agree within error bars. Although the Jason-1/2 data are well sampled, seasonal subsets of spring and autumn data (not shown) indicate no statistically significant differences.

Sentinel-3's SAR mode processing (red line in Fig. 14) has a higher signal-to-noise ratio than conventional altimetry. Previous studies have concluded that the beam-limited footprint of a SAR altimeter should eliminate the spectral bump seen in conventional pulse-limited altimeters, as demonstrated using Cryosat-2 data in the Tropical Pacific [*Dibarboure et al.*, 2014] and in a global assessment of Sentinel-3 data [*Vergara et al.*, 2017]. In this case, as well, we find that Sentinel-3 spectra show no evidence of a spectral bump. However, the short Sentinel-3 record implies large uncertainties, and Sentinel-3 spectra are formally consistent with the ALES-processed Jason-1/2 spectra, both for low wavenumbers and for the highest resolved wavenumbers. We note that this agreement could be specific to the geographic region, perhaps indicative of residual geoid errors, which are particularly significant in coastal regions with high bathymetric variability, such as the CCS.

The AltiKa spectrum (orange line in Fig. 14) agrees with the Jason-1/2 and Sentinel-3 spectra for length scales $L \gtrsim 30$ km. At shorter scales, AltiKa displays a classic spectral bump [*Dibarboure et al.*, 2014; *Raynal et al.*, 2018], albeit with a lower noise floor than is found in either Sentinel-3 or Jason-1/2.

Sentinel-3 data typically indicate red spectra at high wavenumbers in high swell conditions [*Boy et al.*, 2017]. California Current swell varies seasonally, but significant wave heights are typically less than 3 m [*Villas Bôas et al.*, 2017], and in this analysis, we find the high-wavenumber segment of the spectrum to be white. (However, as noted in section 3.2, it would be red if we limited ourselves to using data interpolated onto a common grid.) The low noise floor in AltiKa relative to Sentinel-3 could be an indication that for this region, the Sentinel-3 white noise floor is influenced by inadequate removal of the high-wavenumber geoid, which might be improved as the record grows longer.

All three altimeter products are largely in agreement within statistical uncertainties for scales larger than ~30 km, with steep low-wavenumber spectra with slopes near k^{-4}, as has also been reported in global assessments [e.g., *Stammer*, 1997; *Le Traon et al.*, 2008; *Xu and Fu*, 2012]. For scales shorter than 50 km, the spectra gradually flatten out to slopes near k^{-1}. The agreement suggests the possibility that in the 30-70 km range, the new altimeter products are identifying reproducible characteristics of the wavenumber spectra, albeit with the caveat that these similarities could be coincidental, since the spectral structures at higher wavenumbers differ significantly (with a strong spectral bump in AltiKa, a moderate two-tiered flattening in the ALES-processed Jason 1-2 data, and no spectral bump in Sentinel-3).

The LLC 4320 model sea surface height spectra (green lines in Fig. 14) agree with altimeter spectra for scales $L \gtrsim 125$ km but are steeper at higher wave numbers. The model spectrum based on model-hourly data (solid green line) becomes less steep around $L \simeq 70$ km. At higher wavenumbers, for scales less than ~25–50 km, the model spectrum is expected to be red as suggested in Fig. 11) because of the grid-scale diffusion in the model. The differences in spectral energy in the model-derived results relative to altimetric spectra are not fully understood and could be due to the model SSH having low energy at high wavenumbers, interannual variability not accounted for by the 1-year LLC 4320 simulation or the altimetry reporting too much energy, perhaps associated with residual geoid or mean sea surface effects in the altimeter data.

6 Diagnosing geostrophic velocity from sea surface height

We used the model to further explore the scale dependence of estimating geostrophic velocity from sea surface height. Fig. 15 shows the power spectral density of the meridional velocity component v along 32°N, together with geostrophic velocity v_g estimated using equation (4), as well as the coherence and phase for both hourly and daily-averaged estimates from the full year of model output. The spectra estimated from hourly data compare reasonably well between 300 km and 125 km, corresponding roughly to the balanced flow regime of the model (Fig. 15, red lines in left panel). The coherence is significant and greater than about 0.4 for scales larger than 125 km, with zero phase lag, implying that these are largely the same quantity (Fig. 15, red lines in right panels). An exception is the coherence dip at 150 km, together with a phase shift, that are hard to interpret. The model line 90 KE spectra show a drop in the vortex KE components at about this length scale (Fig. 6). One possibility is that the coherence dip results from a wavelength of the baroclinic tide. At scales smaller than 125 km, there is a large phase shift between v and v_g, but the coherence becomes marginal to insignificant. The spectra estimated from daily-averaged data compare well at all length scales, with high coherence and near-zero phase shift (Fig. 15, blue lines). This reinforces the earlier finding shown in Fig. 6 (upper left panel) that the daily-averaged model KE spectrum is consistent with geostrophic balanced flow. We found similar results using the zonal component along 122°W (not shown).

Examining the LLC 4320 model in the Kuroshio extension region, *Torres et al.* [2018] found seasonality in diagnosing geostrophic velocity from SSH in the Kuroshio region (their Fig. 5) as originally suggested by *Rocha et al.* [2016b]. That does not appear to be the case in the CCS region of the LLC model. Looking at seasonal estimates (not shown), daily-averaged v and v_g have the same seasonality shown in Fig. 11 (right panel), but they track each other in each season, as in the annual average shown in Fig. 15. The seasonal estimates of hourly v and v_g have seasonality at high wavenumbers (not shown), but not in the balanced range from 300 km to 125 km. Most importantly, the discontinuity in the v and v_g hourly spectra occurs at the same wavenumber, around 125 km, in all seasons. Thus the CCS region provides a strong contrast to the Kuroshio Extension region: it exhibits weaker mesoscale energy and seasonality, together with a very short balanced regime. Although the RMS velocity gradient statistics shown in Fig. 10 indicate a seasonal cycle, the amplitude is small compared to that shown for the Kuroshio Extension region [*Rocha et al.*, 2016b].

7 Discussion and summary

We have used high-resolution altimetry, in situ velocity observations and a high-resolution numerical simulation in order to examine the contributions to horizontal velocity and sea surface height variance in the transition from meso- to submesoscales (from 200 km to 10 km) in the southern California Current. In this region, geostrophic flow can be characterized by the local Rossby internal deformation radius of ~30 km [*Chelton et al.*, 1998]. Smaller eddies with diameters 1-2 × the deformation radius form near the coast and propagate offshore [e.g., *Chenillat et al.*, 2018]; larger eddies with diameters ~100 km are observed offshore [*Chelton et al.*, 2007]. Additionally, even larger scale features such as the Southern California Eddy (~300 km), a recirculation of the California Current offshore of the U.S.-Mexico border [e.g., *Lynn and Simpson*, 1987], contribute to the velocity variance at large scales. Ageostrophic motions (e.g., inertia-gravity waves, mixed layer instabilities, Langmuir cell convection, filaments, fronts, etc.) are particularly important in the submesoscale range because they typically project onto small scales and result in flatter spectra. Internal waves, however, such as the internal tide, can project onto large scales; [*Rocha et al.*, 2016a] found that waves projected onto horizontal scales as large as 150 km in Drake Passage. The mixed layer deformation radius [*Thomas and Ferrari*, 2008] is an important scale for the submesoscale. Although mixed layer depth varies over the CCS region, it is generally less than 100 m, and so the mixed layer deformation radius is of order 1-2 km, below the 10 km resolution of the ADCP observations.

Kinetic energy spectra estimated from a high-resolution numerical simulation with embedded tides and from in situ velocity observations from shipboard ADCP transects follow an approximately -2 power law at scales from 100 km to 10 km. A Helmholtz spectral decomposition was used to separate rotational from divergent KE components, and a vortex-wave decomposition was used to discriminate between geostrophically balanced and unbalanced contributions to KE spectra. These methods, applied here as in prior studies [e.g., *Bühler et al.*, 2014; *Rocha et al.*, 2016a; *Qiu et al.*, 2018], invoke a number of assumptions (Section 2). The most limiting are that the rotational and divergent components are statistically independent (Helmholtz decomposition) and that the southern CCS internal wave field can be characterized by the GM [*Garrett and Munk*, 1972] internal wave spectrum and that all divergent flow is due to internal waves (vortex-wave decomposition). At large scales ($L > 70$ km), the observed KE is dominated by balanced geostrophic motions; ageostrophic motions begin to contribute equally at scales $L < 40$ km. For the observations, slope alone does not distinguish the transition from balanced to unbalanced flow dominance, as the diagnosed vortex and wave contributions each have -2 slopes over a broad range of scales from 200 to 10 km. In the model, KE is dominated by geostrophically balanced motions for $L > 125$ km; ageostrophic motions are significant at shorter scales and dominate for $L < 50$ km. The diagnosed vortex and wave contributions estimated from model-hourly spectra each have -2 slopes over the submesoscale range of scales from 100 to 10 km. The model vortex components have less submesoscale KE than observed; the model wave components have more submesoscale KE than observed. We note, however, that the model time series is short, one year, compared to the 11-year time series for the ADCP and could underestimate the balanced motions, which have longer periods than IGW as well as interannual variability.

SSH variance spectra estimated from three altimeter data sets were in agreement for length scales longer than ~30 km. They agreed with the spectra estimated from model-hourly SSH for scales longer than ~125 km, corresponding to the wavenumber range where balanced geostrophic flow dominated the model KE spectra. The spectral slope of the altimeter estimates was about -4 for longer length scales $L \gtrsim 70$ km, consistent with the -2 slopes of the KE spectra estimated from the ADCP observations and corresponding to the wavenumber range where balanced geostrophic flow dominated the ADCP spectra.

The ADCP results in the CCS are similar to those for ADCP observations in the NEC region of the western North Pacific analyzed by *Qiu et al.* [2017]. In both the southern CCS and the NEC, the transition from geostrophically balanced to unbalanced flows occurs at longer length scales, 70 km and 200 km, respectively, than in the strong jets where the transition occurs at scales from 15 km to 40 km [e.g., *Callies and Ferrari*, 2013; *Rocha et al.*, 2016a; *Qiu et al.*, 2018]. Also in contrast with the strong jets, in both the CCS and NEC regions there is no discernible change in spectral slope at the transition; the slope remains about -2, primarily because the mesoscale energy level at longer length scales is weak compared to the submesoscale turbulence and IGW that dominate at shorter scales. The KE spectral slopes in both regions change very little with depth; in particular, the depth-dependence is inconsistent with surface QG theory that predicts spectral slope to steepen rapidly with depth. Unlike the NEC, the CCS transition scale increased with depth in the upper 250 m, likely due to increasing IGW contributions in the thermocline. In the NEC the transition scale remains constant through the upper 300 m and decreases at deeper depths (deeper than sampled in the CCS) due to the sub-thermocline eddy-forced North Equatorial Undercurrent jets. In both regions, no significant seasonality is observed in the total KE spectra, but when decomposed, there is significant seasonality in the components. In the CCS, the ADCP vortex spectra have more energy in winter while in the NEC, the ADCP wave spectra have more energy in summer.

The model allowed a more systematic exploration of the seasonality. Model estimates of RMS vertical vorticity, lateral rate of strain and horizontal divergence indicate that submesoscale turbulence and waves undergo out-of-phase seasonal cycles; submesocale turbulence peaks in late winter/early spring and inertia-gravity waves peak in late summer/early fall. The in situ observations show weaker seasonality than the model. Total KE from ADCP transects has insignificant seasonality. The submesoscale ADCP KE vortex component has weak but significant seasonality, peaking in winter. The submesoscale ADCP KE wave component, however, lacks a statistically significant seasonality. The altimeter data also did not exhibit a statistically significant seasonality. For the ADCP, this lack could be due to insufficient sampling within the summer mixed layer, which lies above the shallowest depth bin of the ADCP. Likewise, for altimetry, this could be a sign that even with many years of ALES-processed Jason data, noise levels remain too high to discern seasonal patterns. Alternatively, it could be that the model overestimates the IGW variability in the CCS. The phase cancellation in the CCS indicated by the numerical simulation is similar to results from the same simulation for the Kuroshio Extension region [*Rocha et al.*, 2016b]. The global LLC 4320 analysis by *Qiu et al.* [2018] finds that this phase cancellation occurs in the model throughout most of the ocean and is due to the occurrence of mixed layer instability in winter and trapping of unbalanced motions in shallow mixed layers in summer. The *Qiu et al.* [2018] study also indicates that seasonality in the CCS region of the LLC 4320 simulation (from about 30°N to 40°N) is weaker than most other regions.

Our model calculations suggest that geostrophic velocity can be estimated from SSH over the model's balanced motion regime, for scales greater than about 125 km. The observations find a larger balanced regime, for scales greater than 70 km, confirmed by ADCP KE spectra and SSH variance spectra from 3 different altimeter products. Both observations and model indicate weak to insignificant seasonality in the balanced regime. With respect to high-resolution altimeters such as SWOT, our results for the southern CCS indicate a transition in SSH spectral slope, with flatter SSH spectra for scales smaller than about 70 km, consistent with the ADCP transition from balanced to unbalanced motion. This suggests that the limit on diagnosing geostrophic velocity from SSH is about 70 km in the southern California Current and is set by the ocean dynamics of the region rather than the resolution of the altimeter.

Acknowledgments

This research was funded by NASA (NNX13AE44G, NNX13AE85G, NNX16AH67G, NNX16AO5OH). We thank Dr. Sung Yong Kim for providing the high frequency radar spectral estimates and the two anonymous reviewers for providing useful comments and suggestions that greatly improved the manuscript. High-Frequency ALES data for Jason-1 and Jason-2 altimeters are available upon request https://openadb.dgfi.tum.de/en/contact/ALES. Both AltiKa and Sentinel-3 altimeter products were produced and distributed by the Copernicus Marine and Environment Monitoring Service (CMEMS) (http://www.marine.copernicus.eu). D.M. worked on the modeling component of this study at the Jet Propulsion Laboratory (JPL), California Institute of Technology, under a contract with the National Aeronautics and Space Administration (NASA). High-end computing resources were provided by the NASA Advanced Supercomputing (NAS) Division of the Ames Research Center. The LLC output can be obtained from the ECCO project (ftp://ecco.jpl.nasa.gov/ECCO2/LLC4320/). The ADCP data are available at the Joint Archive for Shipboard ADCP data (JASADCP)

(http://ilikai.soest.hawaii.edu/sadcp).

References

Bendat, J., and A. Piersol (2010), *Random data: Analysis and Measurement Procedures*, 4th ed., Wiley 604 pp.

Birol, F., M. Cancet, and C. Estournel (2010), Aspects of the seasonal variability of the Northern Current (NW Mediterranean Sea) observed by altimetry, *J. Mar. Sys.*, *81*, 297–311.

Blumen, W. (1978), Uniform potential vorticity flow: Part II: A Model of wave interactions, *J. Atmos. Sci.*, *35*, 784–789.

Bograd, S. J., T. K. Chereskin, and D. Roemmich (2001), Transport of mass, heat, salt, and nutrients in the southern California Current System: Annual cycle and interannual variability, *J. Geophys. Res.*, *106*(C5), 9255–9275.

Boy, F., T. Moreau, P. Thibaut, P. Rieu, J. Aublanc, N. Picot, P. Femenias, and C. Mavrocordatos (2017), New stacking method for removing the SAR sensitivity to swell, in *Ocean Surface Topography Science Team Meeting*, Miami, https://meetings.aviso.altimetry.fr/fileadmin/user_upload/IPM_02_SCOOP_OSTST_2017_v1c.pdf.

Brannigan, L., D. P. Marshall, A. Naveira Garabato, and A. G. Nurser (2015), The seasonal cycle of submesoscale flows, *Ocean Modelling*, *92*, 69–84.

Buckingham, C. E., A. C. Naveira Garabato, A. F. Thompson, L. Brannigan, A. Lazar, D. P. Marshall, A. J. George Nurser, G. Damerell, K. J. Heywood, and S. E. Belcher (2016), Seasonality of submesoscale flows in the ocean surface boundary layer, *Geophysical Research Letters*, *43*(5), 2118–2126, doi:10.1002/2016GL068009, 2016GL068009.

Bühler, O., J. Callies, and R. Ferrari (2014), Wave–vortex decomposition of one-dimensional ship-track data, *J. Fluid. Mech.*, *756*, 1007–1026.

Callies, J., and R. Ferrari (2013), Interpreting energy and tracer spectra of upper-ocean turbulence in the submesoscale range (1–200 km), *J. Phys. Oceanogr.*, *43*, 2456–2474.

Callies, J., R. Ferrari, J. Klymak, and J. Gula (2015), Seasonality in submesoscale turbulence, *Nat Commun*, *6*, 6862, doi:10.1038/ncomms7862.

Capet, X., J. C. McWilliams, M. J. Molemaker, and A. F. Shchepetkin (2008), Mesoscale to Submesoscale Transition in the California Current System. Part II: Frontal Processes, *J. Phys. Oceanogr.*, *38*(1), 44–64, doi:10.1175/2007JPO3672.1.

Charney, J. (1971), Geostrophic turbulence, *J. Atmos. Sci.*, *28*, 1087–1095.

Chelton, D. B., and M. G. Schlax (2003), The accuracies of smoothed sea surface height fields constructed from tandem satellite altimeter datasets, *Journal of Atmospheric and Oceanic Technology*, *20*(9), 1276–1302, doi:10.1175/1520-0426(2003)020<1276:TAOSSS>2.0.CO;2.

Chelton, D. B., R. A. deSzoeke, M. G. Schlax, K. El Naggar, and N. Siwertz (1998), Geographical variability of the first-baroclinc Rossby radius of deformation, *J. Phys. Oceanogr.*, *28*, 433–460.

Chelton, D. B., M. G. Schlax, R. M. Samelson, and R. A. de Szoeke (2007), Global observations of large oceanic eddies, *Geophys. Res. Lett.*, *34*, L15,606, doi: doi:10.1029/2007GL030812, 2007.

Chenillat, F., P. J. S. Franks, X. Capet, P. Riviere, N. Grima, B. Blanke, and V. Combes (2018), Eddy properties in the Southern California Current System, *Ocean Dynamics*, *68*, 761–777, doi:https://doi.org/10.1007/s10236-018-1158-4.

Chereskin, T. K., and A. J. Harding (1993), Modeling the performance of an acoustic Doppler current profiler, *J. Atmos. Oceanic Technol.*, *10*(1), 41–63.

Chereskin, T. K., and C. L. Harris (1997), Shipboard acoustic Doppler profiling during the WOCE Indian Ocean Expedition: I10, *Tech. Rep. SIO-97-14*, Scripps Inst. of Oceanogr.

Chereskin, T. K., and M. Trunnell (1996), Correlation scales, objective mapping, and absolute geostrophic flow in the California Current, *Journal of Geophysical Research: Oceans*, *101*(C10), 22,619–22,629, doi:10.1029/96JC02004.

Dibarboure, G., F. Boy, J. D. Desjonqueres, S. Labroue, Y. Lasne, N. Picot, J. C. Poisson, and P. Thibaut (2014), Investigating short-wavelength correlated errors on low-resolution mode altimetry, *J. Atmos. Oceanic Technol.*, *31*, 1337–1362, doi:10.1175/JTECH-D-13-00081.1.

Durand, F., D. Shankar, F. Birol, and S. S. C. Shenoi (2008), An algorithm to estimate coastal currents from satellite altimetry: A case study for the East India Coastal Current, *J. Oceanogr.*, *64*, 831–845.

EUMETSAT (2017), Sentinel-3 SRAL Marine User Handbook, *Tech. Rep. EUM/OPS-SEN3/MAN/17/920901*, EUMETSAT, Eumetsat-Allee 1, D-64295 Darmstadt, Germany.

Firing, E., and J. M. Hummon (2010), Ship-mounted acoustic Doppler current profilers, in *The GO-SHIP Repeat Hydrography Manual: A Collection of Expert Reports and Guidelines*, edited by E. Hood, C. Sabine, and B. Sloyan, IOCCP Report Number 14, ICPO Publication Series Number 134, Available online at: http://www.go-ship.org/HydroMan.html.

Forget, G., J.-M. Campin, P. Heimbach, C. Hill, R. Ponte, and C. Wunsch (2015), ECCO version 4: an integrated framework for non-linear inverse modeling and global ocean state estimation, *Geosci. Model Dev.*, *8*, 3071–3104.

Fu, L.-L., and C. Ubelmann (2014), On the transition from profile altimeter to swath altimeter for observing global ocean surface topography, *Journal of Atmospheric and Oceanic Technology*, *31*(2), 560–568, doi:10.1175/JTECH-D-13-00109.1.

Garrett, C. J. R., and W. H. Munk (1972), Space-time scales of internal waves, *Geophys. Flud. Dyn.*, *2*, 225–264.

Gay, P. S., and T. K. Chereskin (2009), Mean structure and seasonal variability of the poleward undercurrent off southern California, *Journal of Geophysical Research: Oceans*, *114*(C2), n/a–n/a, doi:10.1029/2008JC004886, c02007.

Heslop, E. E., A. Sánchez-Román, A. Pascual, D. Rodríguez, K. A. Reeve, Y. Faugère, and M. Raynal (2017), Sentinel-3a views ocean variability more accurately at finer resolution, *Geophysical Research Letters*, *44*(24), 12,367–12,374, doi:10.1002/2017GL076244.

Hill, C., D. Menemenlis, B. Ciotti, and C. Henze (2007), Investigating solution convergence in a global ocean model using a 2048-processor cluster of distributed shared memory machines, *Scientific Programming*, *15*, 107–115.

Kim, S.-Y., J. Terrill, B. D. Cornuelle, B. Jones, L. Washburn, M. A. Moline, J. D. Paduan, N. Garfield, J. L. Largier, G. Crawford, and P. M. Kosro (2011), Mapping the U.S. West Coast surface circulation: A multiyear analysis of high-frequency radar observations, *J. Geophys. Res.*, *116*, 10.1029/2010JC006669.

Lapeyre, G. (2009), What vertical mode does the altimeter reflect? on the decomposition in baroclinic modes and on a surface-trapped mode, *J. Phys. Oceanogr.*, *39*(11), 2857–2874, doi:10.1175/2009JPO3968.1.

Lapeyre, G., and P. Klein (2006), Dynamics of the upper oceanic layers in terms of surface quasigeostrophy theory, *J. Phys. Oceanogr.*, *36*(2), 165–176, doi:10.1175/JPO2840.1.

Le Traon, P. Y., P. Klein, B. L. Hua, and G. Dibarboure (2008), Do altimeter wavenumber spectra agree with the interior or surface quasigeostrophic theory?, *J. Phys. Oceanogr.*, *38*, 1137–1142.

Lynn, R. J., and J. J. Simpson (1987), The California Current System: The seasonal variability of its physical characteristics, *J. Geophys. Res.*, *92*, 12,947–12,966.

Marshall, J., A. Adcroft, C. Hill, L. Perelman, and C. Heisey (1997), A finite-volume, incompressible Navier Stokes model for studies of the ocean on parallel computers, *J. Geophys. Res.*, *102*, 5753–5766.

Menemenlis, D., J.-M. Campin, P. Heimbach, C. Hill, T. Lee, A. Nguyen, M. Schodlok, and H. Zhang (2008), ECCO2: High resolution global ocean and sea ice data synthesis, *Mercator Ocean Quarterly Newsletter*, *31*, 13–21.

Passaro, M., P. Cipollini, S. Vignudelli, G. D. Quartly, and H. M. Snaith (2014), ALES: A multi-mission adaptive subwaveform retracker for coastal and open ocean altimetry, *Remote Sensing of Environment*, *145*, 173 – 189, doi: https://doi.org/10.1016/j.rse.2014.02.008.

Passaro, M., S. Dinardo, G. D. Quartly, H. M. Snaith, J. Benveniste, P. Cipollini, and B. Lucas (2016), Cross-calibrating ALES, Envisat and Cryosat-2 Delay Doppler: a coastal altimetry study in the Indonesian seas, *Advances in Space Research*, *58*(3), 289–303, doi:10.1016/j.asr.2016.04.011.

Passaro, M., S. K. Rose, O. B. Anderson, E. Boergens, F. M. Calafat, D. Dettmering, and J. Benveniste (2018), Ales+: Adapting a homogenous ocean retracker for satellite altimetry to sea ice leads, coastal and inland waters, *Remote Sensing of Environment*, *211*, 456–471, doi:10.1016/j.rse.2018.02.074.

Qiu, B., S. Chen, P. Klein, H. Sasaki, and Y. Sasai (2014), Seasonal Mesoscale and Submesoscale Eddy Variability along the North Pacific Subtropical Countercurrent, *J. Phys. Oceanogr.*, *44*(12), 3079–3098, doi:10.1175/JPO-D-14-0071.1.

Qiu, B., T. Nakano, S. Chen, and P. Klein (2017), Submesoscale transition from geostrophic flows to internal waves in the northwestern Pacific upper ocean, *Nat Commun*, *8*(14055), doi:doi:10.1038/ncomms14055.

Qiu, B., S. Chen, P. Klein, J. Wang, H. Torres, L.-L. Fu, and D. Menemenlis (2018), Seasonality in transition scale from balanced to unbalanced motions in the world ocean, *J. Phys. Oceanogr.*, *48*, 591–605, doi:10.1175/JPO-D-17-0169.1.

Quartly, G. D., and M. Passaro (2015), Initial examination of AltiKa's individual echoes, *Marine Geodesy*, *38*(Supplement 1), 73–85, doi:10.1080/01490419.2014.984882.

Raney, R. K. (1998), The delay/Doppler radar altimeter, *IEEE Trans. Geosci. Remote Sens.*, *36*, 1578–1588, doi:10.1109/36.718861.

Raynal, M., S. Labroue, T. Moreau, F. Boy, and N. Picot (2018), From conventional to Delay Doppler altimetry: A demonstration of continuity and improvements with the Cryosat-2 mission, *Advances in Space Research*, doi: https://doi.org/10.1016/j.asr.2018.01.006.

Roblou, L., J. Lamouroux, J. Bouffard, M. Le Hénaff, A. Lombard, P. Marsaleix, and P. De Mey (2011), *Coastal altimetry*, chap. Postprocessing altimeter data toward coastal applications and integration into coastal mode, eds. S. Vignudelli, A. Kostianoy, P. Cipollini and J. Benveniste, Springer-Verlag, Berlin.

Rocha, C. B., T. K. Chereskin, S. T. Gille, and D. Menemenlis (2016a), Mesoscale to submesoscale wavenumber spectra in Drake Passage, *J. Phys. Oceanogr.*, *46*, 601–620.

Rocha, C. B., S. T. Gille, T. K. Chereskin, and D. Menemenlis (2016b), Seasonality of submesoscale dynamics in the Kuroshio Extension, *Geophysical Research Letters*, *43*(21), 11,304–11,311, doi:10.1002/2016GL071349, 2016GL071349.

Sasaki, H., and P. Klein (2012), Wavenumber spectra in the North Pacific from a high-resolution realistic simulation, *J. Phys. Oceanogr.*, *42*, 1233–1241.

Sasaki, H., P. Klein, B. Qiu, and Y. H. Sasai (2014), Impact of oceanic-scale interactions on the seasonal modulation of ocean dynamics by the atmosphere, *Nat Commun*, *5*.

Savage, A. C., B. K. Arbic, M. H. Alford, J. K. Ansong, J. T. Farrar, D. Menemenlis, A. K. O'Rourke, J. G. Richman, J. F. Shriver, G. Voet, A. J. Wallcraft, and L. Zamudio (2017), Spectral decomposition of internal gravity wave sea surface height in global models, *J. Geophys. Res.*, *122*(10), 7803–7821, doi:10.1002/2017JC013009.

Shcherbina, A. Y., E. A. D'Asaro, C. M. Lee, J. M. Klymak, M. J. Molemaker, and J. C. McWilliams (2013), Statistics of vertical vorticity, divergence, and strain in a developed submesoscale turbulence field, *Geophysical Research Letters*, *40*(17), 4706–4711.

Smith, W. H. F., E. W. Leuliette, M. Passaro, G. Quartly, and P. F. Cipollini (2017), Covariant errors in ocean retrackers evaluated using along-track cross-spectra, in *Ocean Surface Topography Science Team Meeting*, Miami, https://meetings.aviso.altimetry.fr/fileadmin/user_upload/IPM_08_WHFSmith_Covariant_Errors.pdf.

Stammer, D. (1997), Global Characteristics of Ocean Variability Estimated from Regional TOPEX/POSEIDON Altimeter Measurements, *J. Phys. Oceanogr.*, *27*(8), 1743–1769, doi:10.1175/1520-0485(1997)027<1743:GCOOVE>2.0.CO;2.

Su, Z., J. Wang, P. Klein, A. F. Thompson, and D. Menemenlis (2018), Ocean submesoscales as a key component of the global heat budget, *Nat Commun*, *9*(1), 775, doi:

10.1038/s41467-018-02983-w.

Thomas, L., and R. Ferrari (2008), Friction, frontogenesis and the stratification of the surface mixed layer, *J. Phys. Oceanogr.*, *38*, 2501–2518.

Thompson, A. F., A. Lazar, C. Buckingham, A. C. Naveira Garabato, G. M. Damerell, and K. J. Heywood (2016), Open-ocean submesoscale motions: A full seasonal cycle of mixed layer instabilities from gliders, *Journal of Physical Oceanography*, *46*(4), 1285–1307.

Torres, H. S., P. Klein, D. Menemenlis, B. Qiu, Z. Su, J. Wang, S. Chen, and L.-L. Fu (2018), Partitioning ocean motions into balanced motions and internal gravity waves: a modeling study in anticipation of future space missions, *J. Geophys. Res.*, *123*, doi: https://doi.org/10.1029/2018JC014438.

Vergara, O., R. Morrow, I. Pujol, and G. Dibarboure (2017), Altimetric wavenumber spectra and noise floors, in *Ocean Surface Topography Science Team Meeting*, Miami, https://meetings.aviso.altimetry.fr/fileadmin/user_upload/ERR_04_vergara_ostst.pdf.

Verron, J., P. Sengenes, J. Lambin, J. Noubel, N. Steunou, A. Guillot, N. Picot, S. Coutin-Faye, R. Sharma, R. M. Gairola, D. V. A. Raghava Murthy, J. G. Richman, D. Griffin, A. Pascual, F. Rémy, and P. K. Gupta (2015), The SARAL/AltiKa Altimetry Satellite Mission, *Marine Geodesy*, *0*(ja), 00–00, doi:10.1080/01490419.2014.1000471.

Villas Bôas, A. B., S. T. Gille, M. R. Mazloff, and B. D. Cornuelle (2017), Characterization of the deep water surface wave variability in the California Current region, *Journal of Geophysical Research: Oceans*, *122*(11), 8753–8769, doi:10.1002/2017JC013280.

Wang, D.-P., C. N. Flagg, K. Donohue, and H. T. Rossby (2010), Wavenumber spectrum in the Gulf Stream from shipboard ADCP observations and comparison with altimetry measurements, *J. Phys. Oceanogr.*, *40*, 840–844.

Xu, Y., and L.-L. Fu (2012), The effects of altimeter instrument noise on the estimation of the wavenumber spectrum of sea surface height, *J. Phys. Oceanogr.*, *42*, 2229–2233, doi:10.1175/JPO-D-12-0106.1.

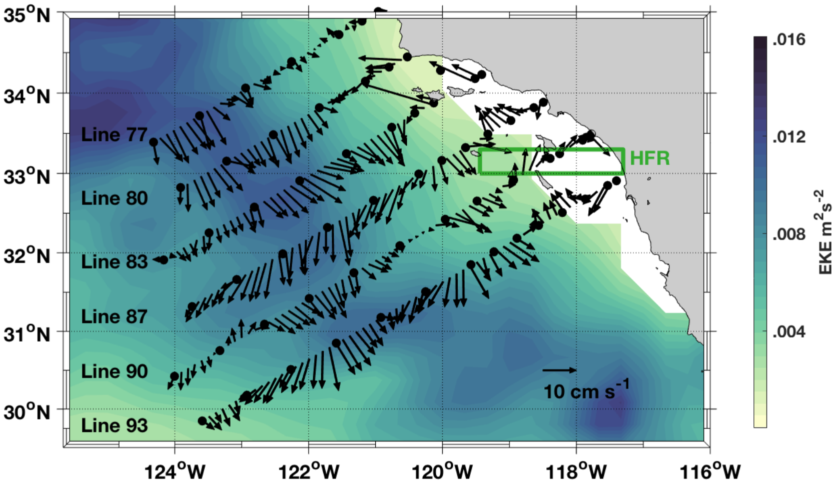
35°N
34°N
33°N
32°N
31°N
30°N
124°W
122°W
120°W
118°W
116°W
Line 77
Line 80
Line 83
Line 87
Line 90
Line 93
HFR
10 cm s^{-1}
.016
.012
.008
.004
EKE m^{2}s^{-2}

Figure 1. Mean (1993-2004) CalCOFI ADCP currents at 20 m depth superposed on eddy kinetic energy estimated from Aviso altimetry for the same time interval. High frequency radar (HFR) estimates were made by *Kim et al.* [2011] for the region denoted by the green box.

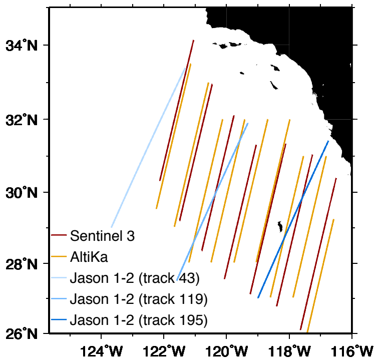
34°N
32°N
30°N
28°N
26°N
124°W
122°W
120°W
118°W
116°W
Sentinel 3
AltiKa
Jason 1-2 (track 43)
Jason 1-2 (track 119)
Jason 1-2 (track 195)

Figure 2. Altimeter ground track segments used for this study, including tracks from Jason-1 and Jason-2 (blues), Sentinel-3 (red), and AltiKa (orange). Sentinel-3 and AltiKa tracks are descending (collected when the satellite is moving southward), and Jason tracks are ascending (satellite moving northward).

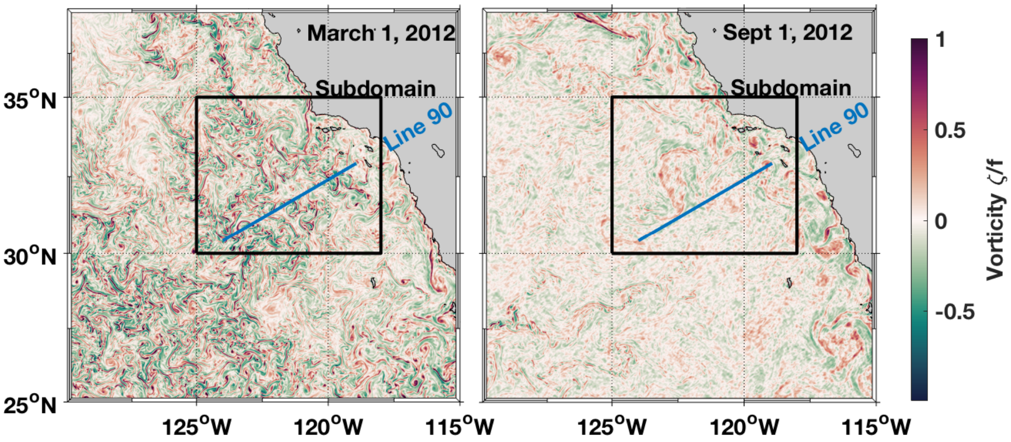
March 1, 2012
Sept 1, 2012
Subdomain
Subdomain
Line 90
Line 90
35°N
30°N
25°N
125°W
120°W
115°W
125°W
120°W
115°W
1
0.5
0
-0.5
Vorticity ζ/f

Figure 3. Snapshots of surface relative vorticity from the LLC 4320 model taken at midnight UTC on March 1, 2012 (left) and Sept. 1, 2012 (right). The blue line corresponds to CalCOFI Line 90. Model KE spectra are estimated along this line for comparison with observations. Model velocity gradient statistics are estimated for the subdomain denoted by the black box.

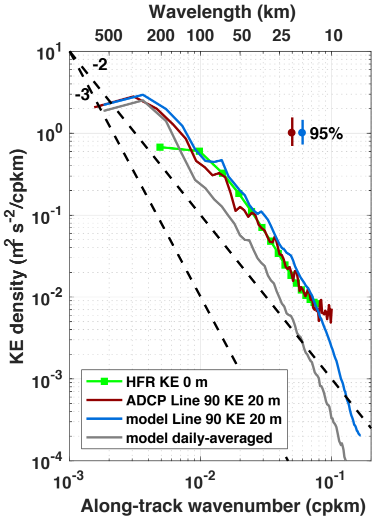

Figure 4. Kinetic energy (KE) spectra at 20-m depth for ADCP (red) and LLC 4320 model-hourly (blue) and model-daily (gray) transects along line 90. Also shown, the KE surface spectrum (green) from high frequency radar (HFR) estimated by *Kim et al.* [2011] for the region denoted by the green box shown in Fig. 1. 95% confidence limits are shown for the ADCP (red) and model-hourly (blue) estimates. Black dashed lines show slopes of −2 and −3 for reference.

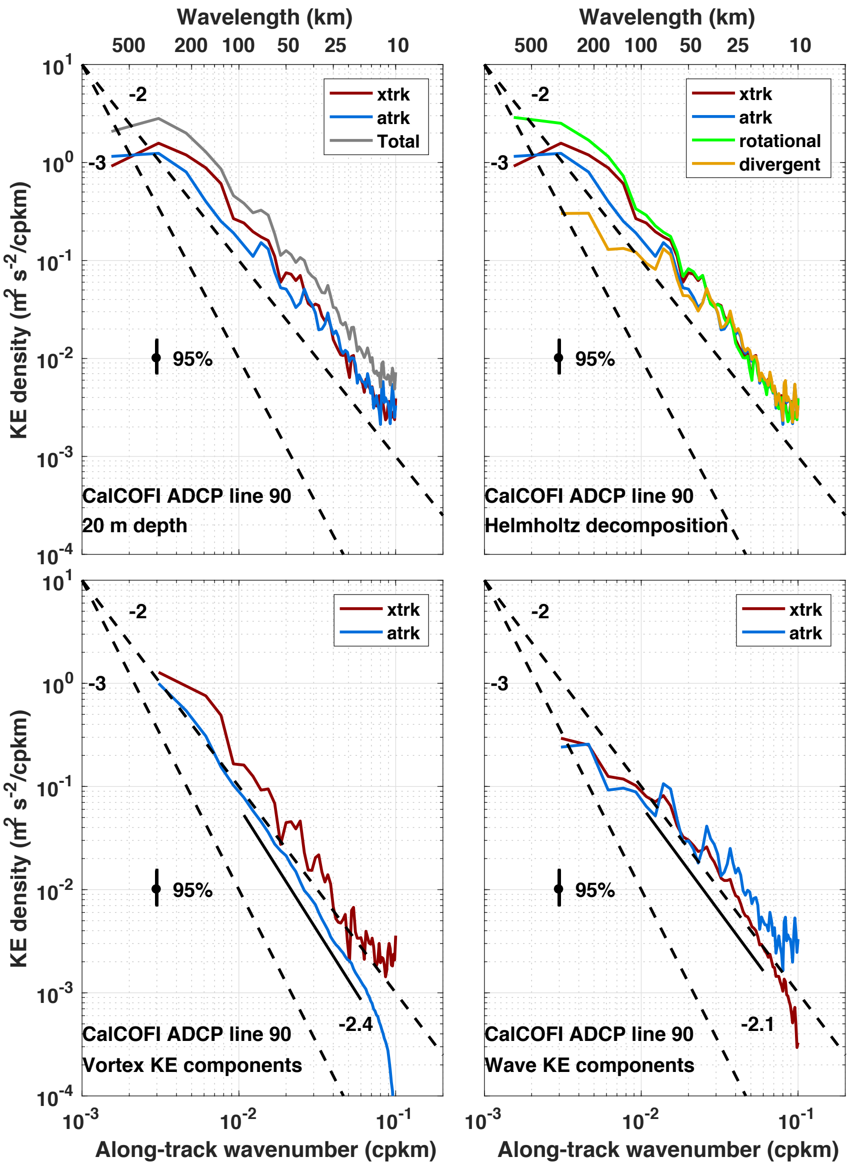

Figure 5. Helmholtz and wave-vortex decompositions of the ADCP KE spectra at 20-m depth for transects along line 90. Upper left: Across-track (red) and along-track (blue) KE components at 20-m depth for ADCP transects. Total (gray) ADCP KE as shown in Fig. 4. Upper right: Across-track (red) and along-track (blue) KE components and the Helmholtz decomposition into rotational (green) and divergent (orange) components. Lower left: Vortex across-track (red) and along-track (blue) components. Lower right: Wave across-track (red) and along-track (blue) components. In all panels, black dashed lines show slopes of −2 and −3 for reference; 95% confidence limits are also shown. In lower panels, the slope of the solid black line is a least squares fit to the KE estimates over the wavenumber range 0.01 to 0.06 cpkm, offset for clarity.

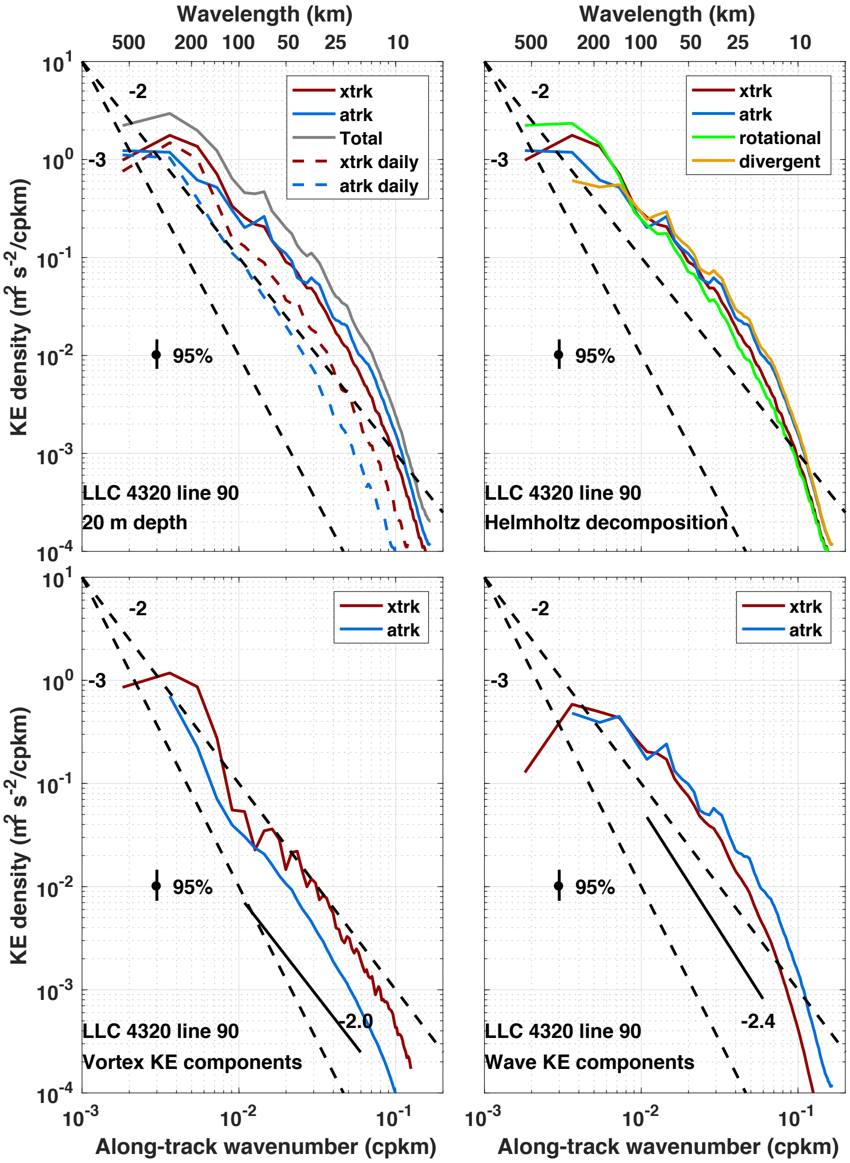

Figure 6. Helmholtz and wave-vortex decompositions of the LLC 4320 model-hourly KE spectra at 20-m depth along line 90. Upper left: Across-track (red) and along-track (blue) KE components at 20-m depth for model-hourly (solid) and model-daily (dashed) transects. Total (gray) model-hourly KE as shown by the blue line in Fig. 4. Upper right: Across-track (red) and along-track (blue) KE components and the Helmholtz decomposition into rotational (green) and divergent (orange) components. Lower left: Vortex across-track (red) and along-track (blue) components. Lower right: Wave across-track (red) and along-track (blue) components. In all panels, black dashed lines show slopes of −2 and −3 for reference; 95% confidence limits are also shown. In lower panels, the slope of the solid black line is a least squares fit to the KE estimates over the wavenumber range 0.01 to 0.06 cpkm, offset for clarity.

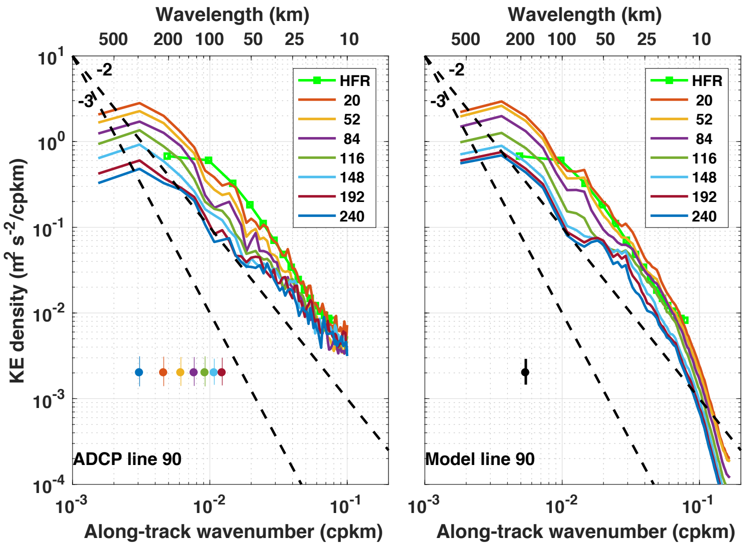

Figure 7. Total KE estimates for ADCP (left) and LLC 4320 model-hourly (right) transects along line 90 are shown for a subset of depth layers. The total KE surface spectrum from high frequency radar (HFR) was estimated by *Kim et al.* [2011] for the region denoted by the green box shown in Fig. 1 and is plotted in both panels. 95% confidence limits are shown for the ADCP (left, color-coded for depth) and model (right, hourly averaged data). Black dashed lines show slopes of −2 and −3 for reference.

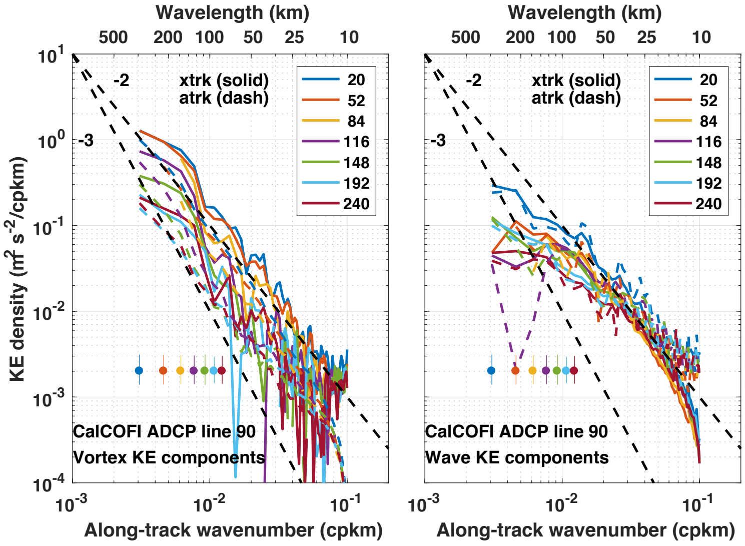

Figure 8. Spectra of vortex (left) and wave (right) KE components for ADCP transects along line 90. Solid lines denote across-track components and dashed lines denote along-track components. Depths are differentiated by color. The 95% confidence limits are shown, color coded by depth. Black dashed lines show slopes of −2 and −3 for reference.

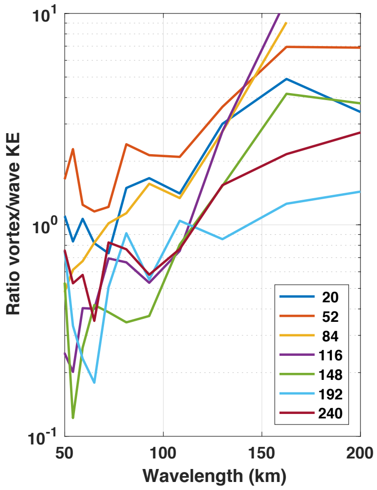

Figure 9. Ratio of vortex:wave KE versus wavelength at multiple depths for the ADCP vortex-wave decompositions shown in Fig. 8. Ratios larger than one are interpreted as dominated by balanced (geostrophic) motions; ratios less than one are interpreted as dominated by ageostrophic motions.

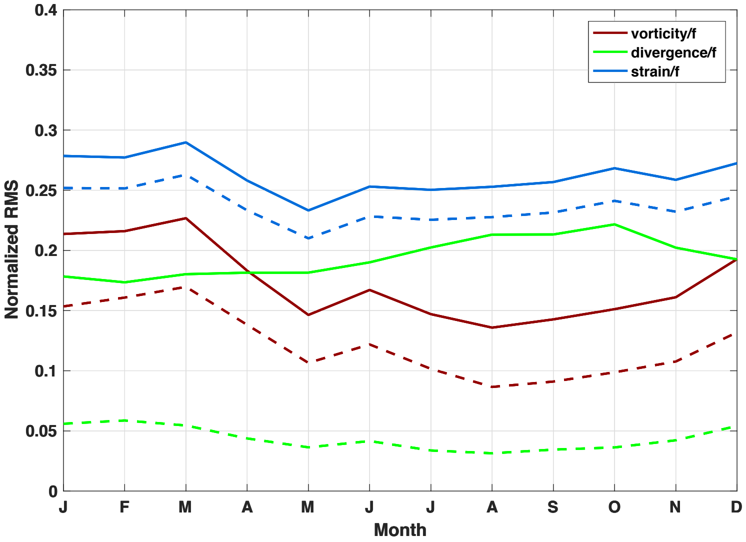

Figure 10. Monthly averages of normalized root-mean-square (RMS) vorticity (red), strain (blue) and divergence (green) estimated at the ocean surface. RMS is averaged over the subdomain shown in Fig. 3 from one year of the 1/48° LLC 4320 model. RMS gradients are normalized by the local Coriolis parameter f. Solid/dashed lines are computed from hourly/daily averages respectively.

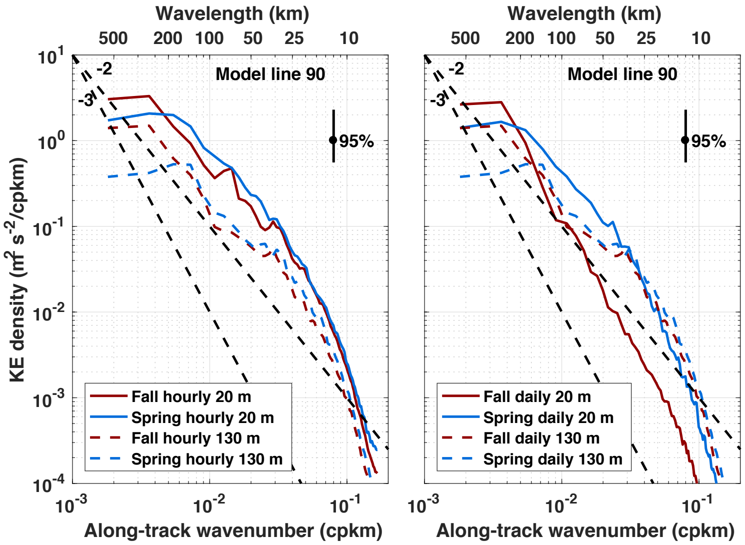

993 **Figure 11.** Seasonal KE spectra from the LLC 4320 model velocity estimates along line 90 for fall (red) 994 and spring (blue). Left panel: KE estimates from hourly averages at depths of 20 m (solid) and 130 m 995 (dashed). Right panel: KE estimates from daily averages at depths of 20 m (solid) and 130 m (dashed). 996 Black dashed lines show slopes of −2 and −3 for reference.

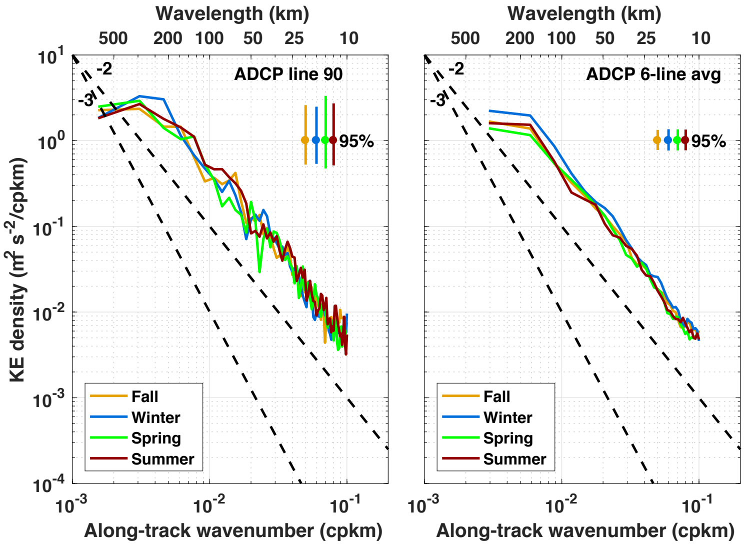

Figure 12. Seasonal averages of total KE at 20 m depth for (left) ADCP transects along line 90 and (right) ADCP transects averaged over all 6 CalCOFI lines. In both panels transects were averaged according to seasons: Fall (Sep/Oct/Nov), Winter (Dec/Jan/Feb), Spring (Mar/Apr/May) and Summer (Jun/Jul/Aug). 95% confidence limits are shown, color coded by season. Black lines show slopes of −2 and −3 for reference.

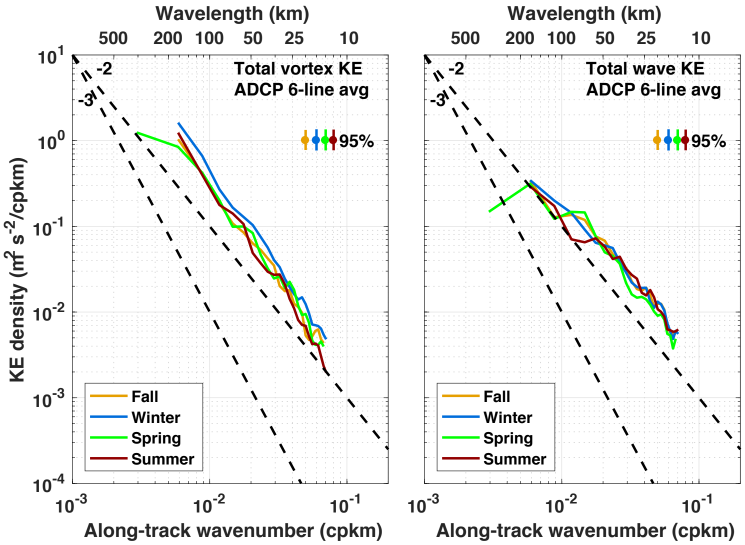

Figure 13. Seasonal averages of total KE decomposed into vortex (left) and wave (right) contributions for ADCP transects at 20-m depth averaged over all 6 CalCOFI lines. Transects were averaged according to seasons: Fall (Sep/Oct/Nov), Winter (Dec/Jan/Feb), Spring (Mar/Apr/May) and Summer (Jun/Jul/Aug). 95% confidence limits are shown, color coded by season. Black lines show slopes of −2 and −3 for reference.

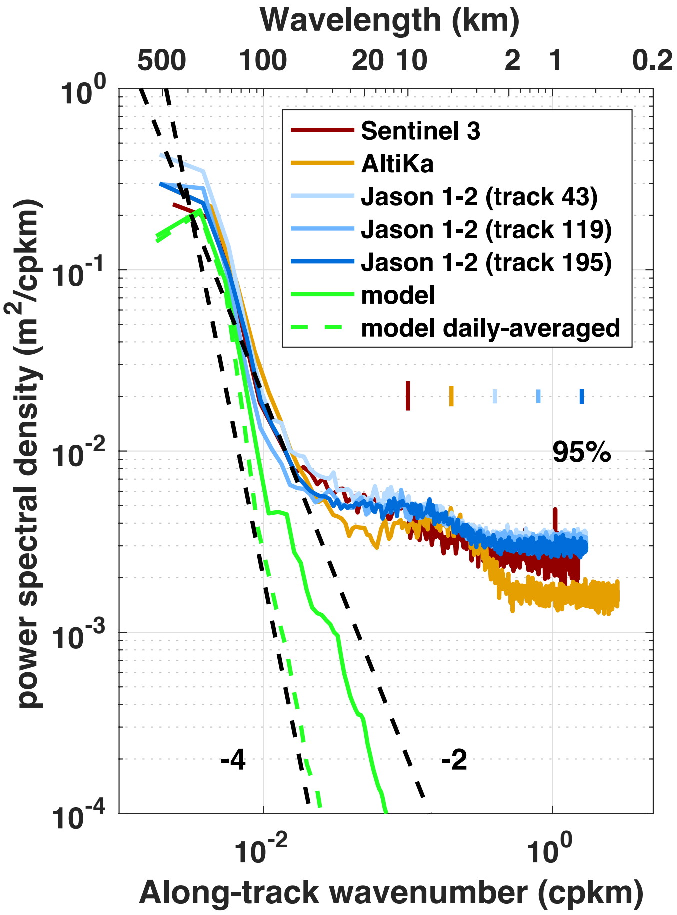

Figure 14. Sea surface height spectra for the California Current altimeter tracks shown in Fig. 2 and for the LLC 4320 model output. For reference, black lines indicate k^{-2} and k^{-4} spectral slopes.

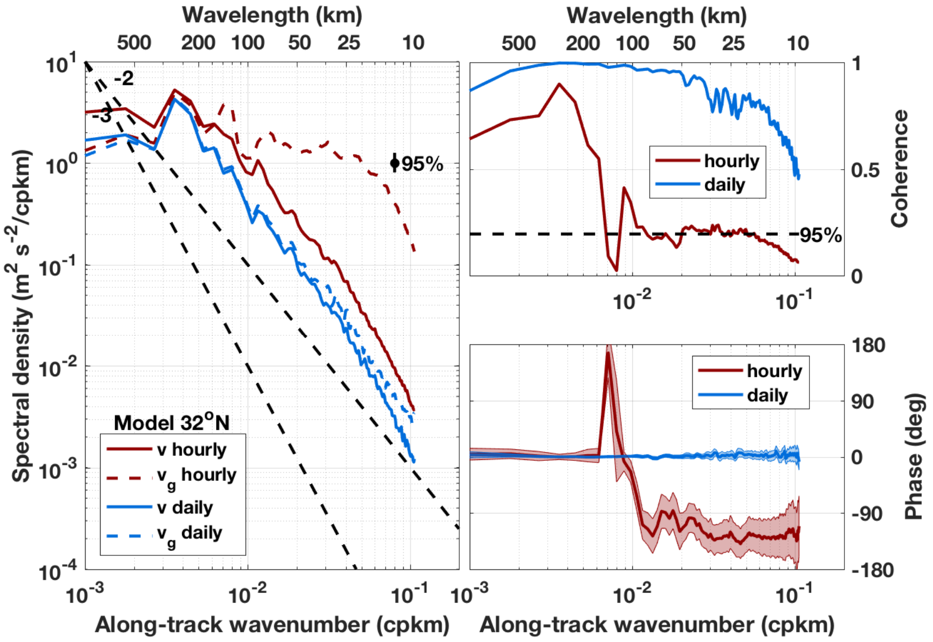

Figure 15. Left: Spectral density of meridional velocity v (colored solid lines) and geostrophic velocity v_g (colored dashed lines) estimated from the LLC 4320 model along latitude 32°N in the subdomain shown in Fig. 3. Black dashed lines show slopes of -2 and -3 for reference. Upper right: Coherence between v and v_g; 95% significance level is shown by the black dashed line. Lower right: Phase between between v and v_g; 95% confidence is denoted by shading. In all panels, values corresponding to hourly and daily-averaged velocities are denoted by red and blue, respectively.

Figure 1.

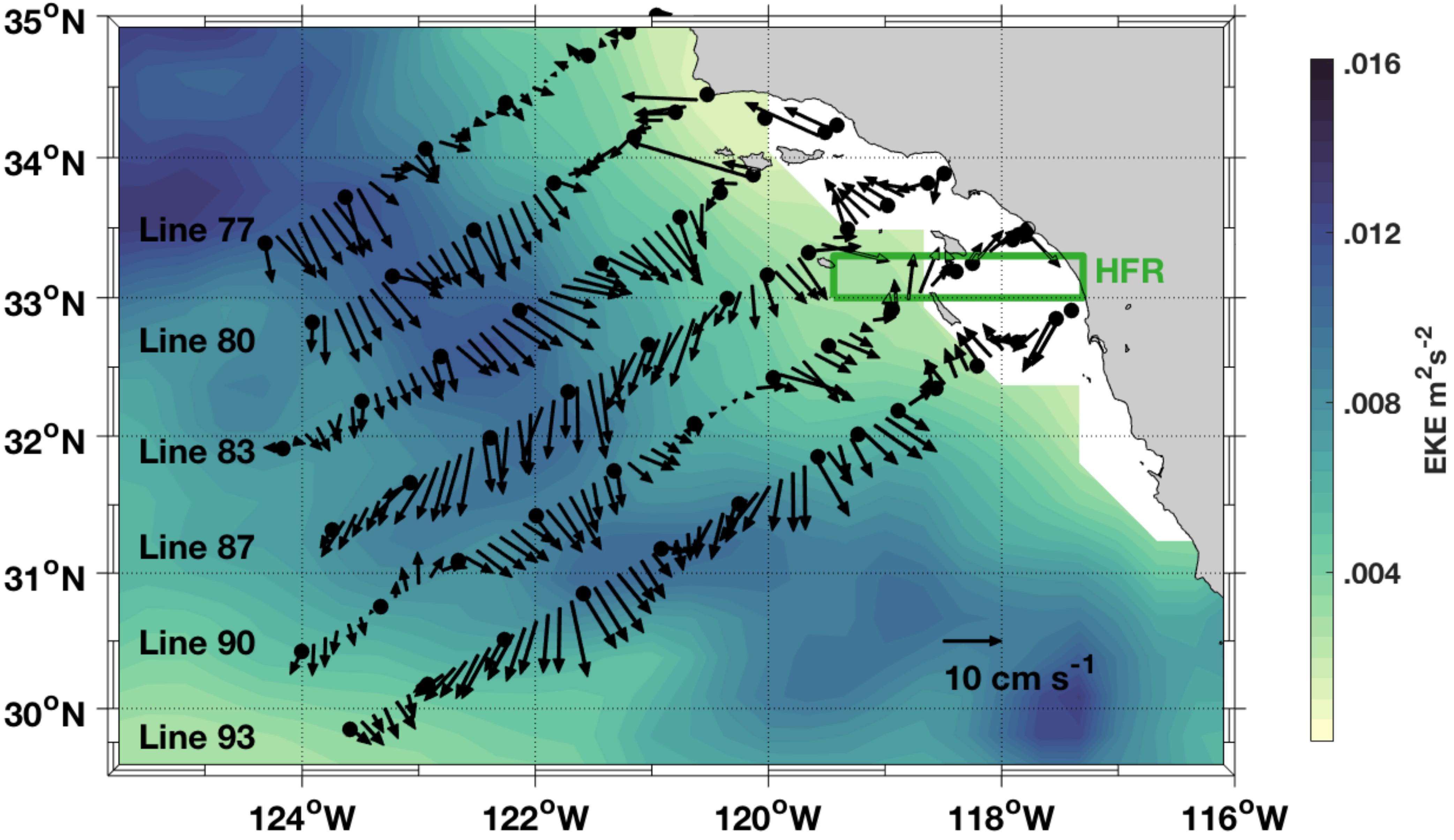
35°N
34°N
33°N
32°N
31°N
30°N
124°W
122°W
120°W
118°W
116°W
Line 77
Line 80
Line 83
Line 87
Line 90
Line 93
HFR
10 cm s^{-1}
.016
.012
.008
.004
EKE m^{2}s^{-2}

Figure 2.

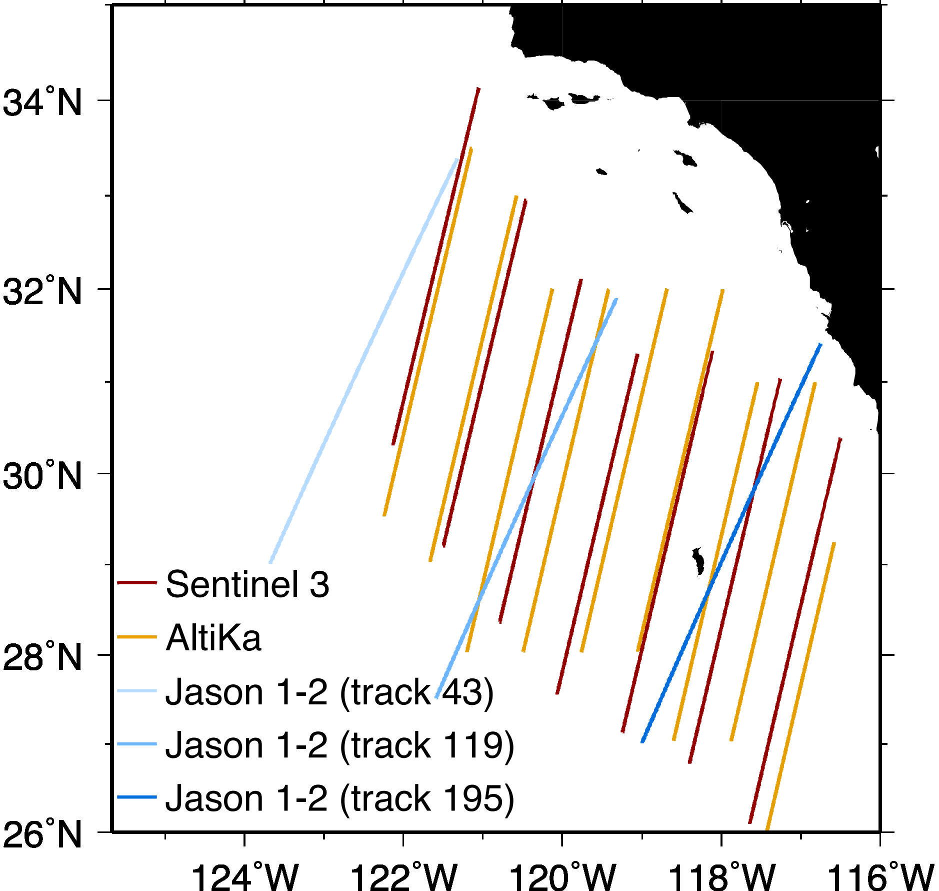
34°N
32°N
30°N
28°N
26°N
124°W
122°W
120°W
118°W
116°W
Sentinel 3
AltiKa
Jason 1-2 (track 43)
Jason 1-2 (track 119)
Jason 1-2 (track 195)

Figure 3.

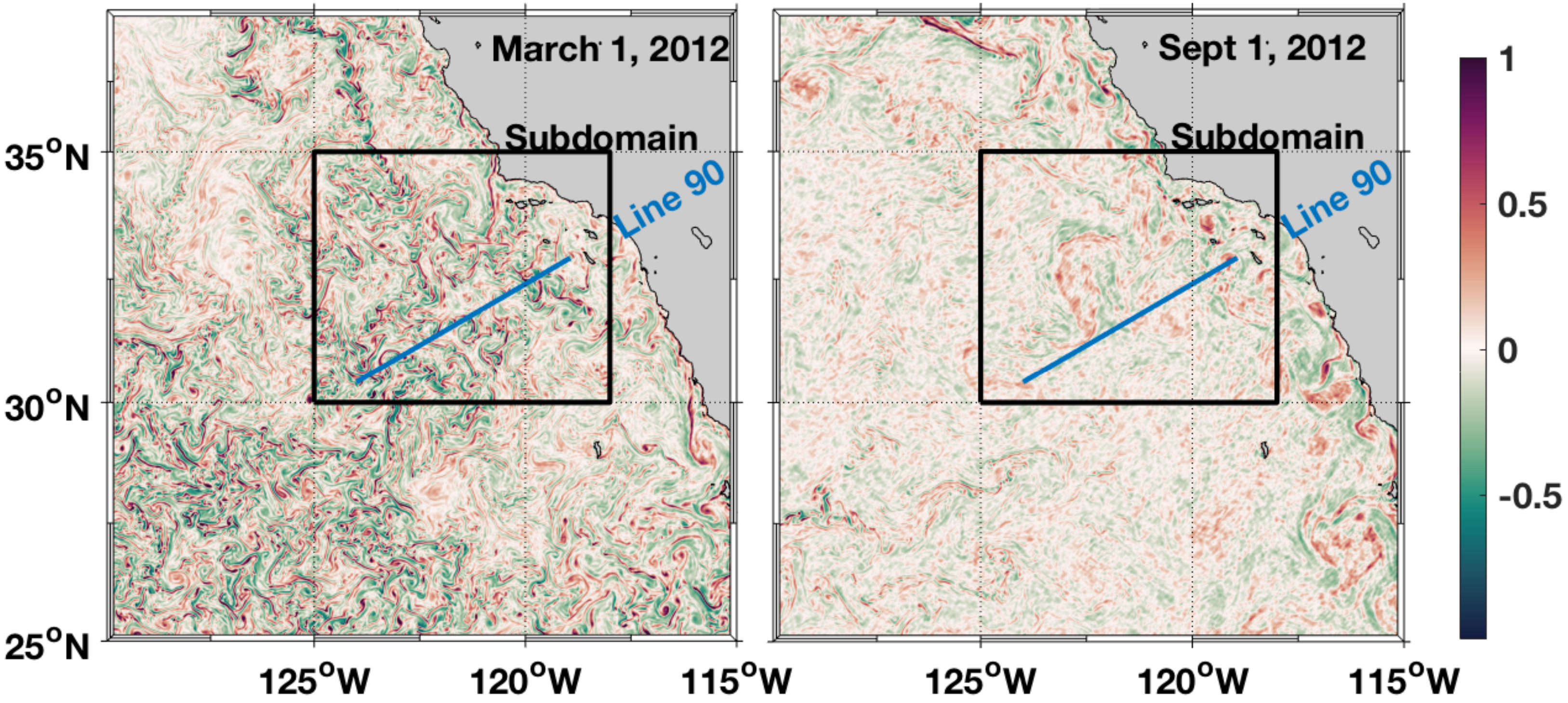
March 1, 2012
Sept 1, 2012
Subdomain
Subdomain
Line 90
Line 90
35°N
30°N
25°N
125°W
120°W
115°W
125°W
120°W
115°W
1
0.5
0
-0.5
Vorticity ζ/f

Figure 4.

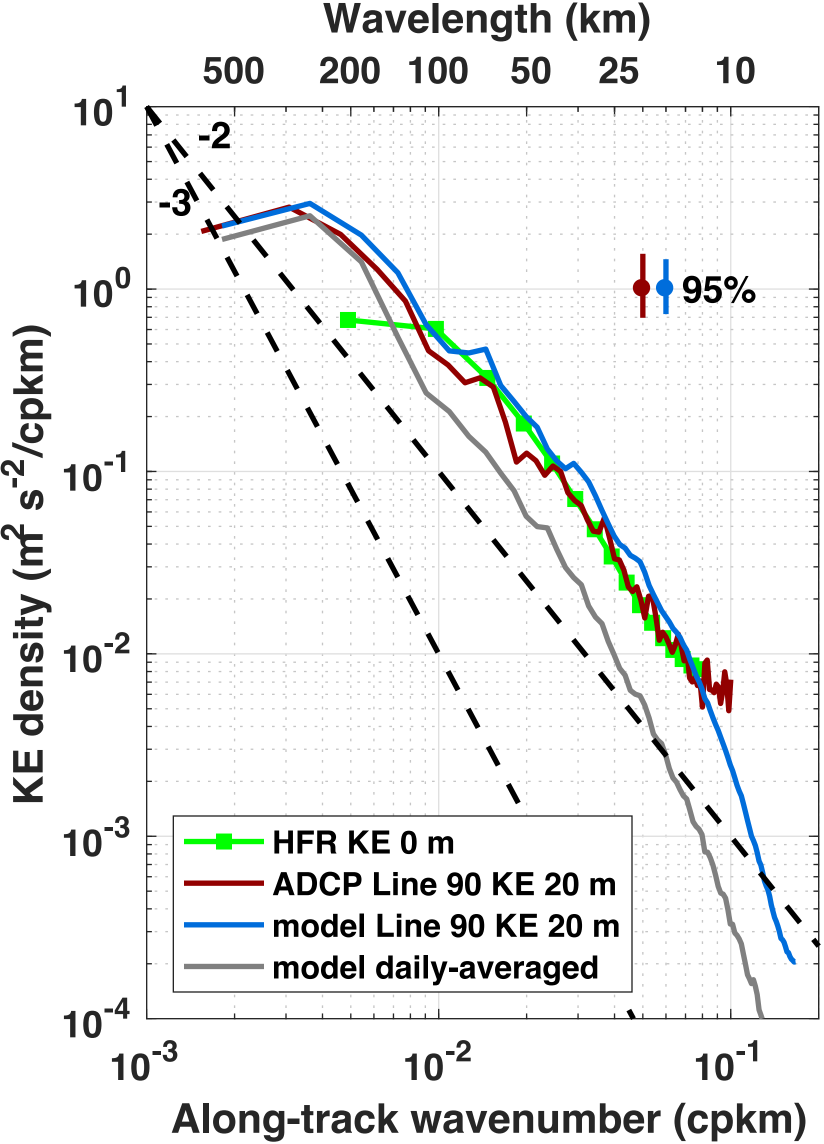
Wavelength (km)
500
200
100
50
25
10
10^1
10^0
10^{-1}
10^{-2}
10^{-3}
10^{-4}
-2
-3
95%
KE density ($m^2 s^{-2}$/cpkm)
HFR KE 0 m
ADCP Line 90 KE 20 m
model Line 90 KE 20 m
model daily-averaged
10^{-3}
10^{-2}
10^{-1}
Along-track wavenumber (cpkm)

Figure 5.

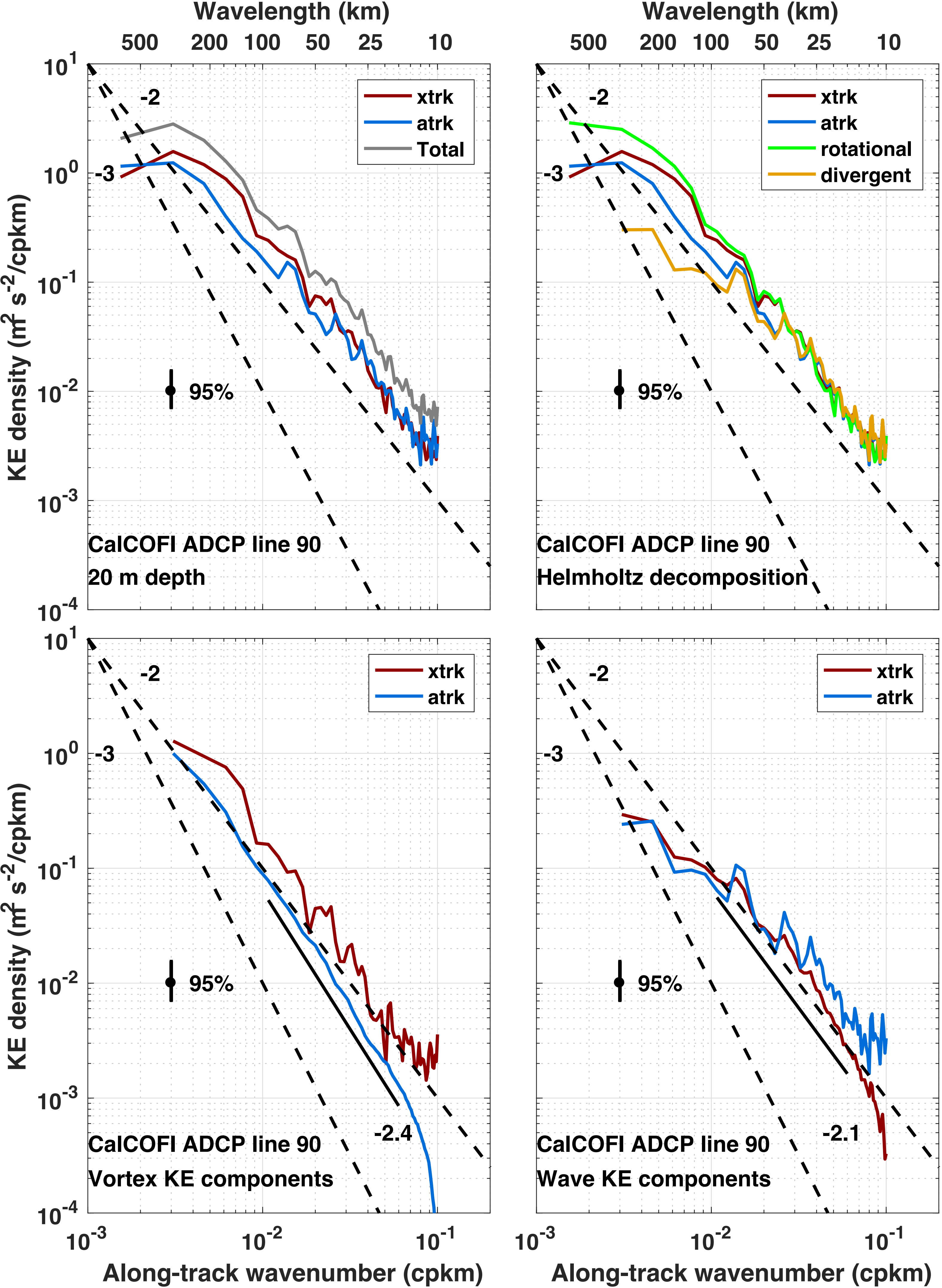
Wavelength (km)
500
200
100
50
25
10
KE density ($m^2 s^{-2}$/cpkm)
10^1
10^0
10^{-1}
10^{-2}
10^{-3}
10^{-4}
-2
-3
xtrk
atrk
Total
95%
CalCOFI ADCP line 90
20 m depth
Wavelength (km)
500
200
100
50
25
10
-2
-3
xtrk
atrk
rotational
divergent
95%
CalCOFI ADCP line 90
Helmholtz decomposition
KE density ($m^2 s^{-2}$/cpkm)
10^1
10^0
10^{-1}
10^{-2}
10^{-3}
10^{-4}
-2
-3
xtrk
atrk
95%
-2.4
CalCOFI ADCP line 90
Vortex KE components
10^{-3}
10^{-2}
10^{-1}
Along-track wavenumber (cpkm)
-2
-3
xtrk
atrk
95%
-2.1
CalCOFI ADCP line 90
Wave KE components
10^{-3}
10^{-2}
10^{-1}
Along-track wavenumber (cpkm)

Figure 6.

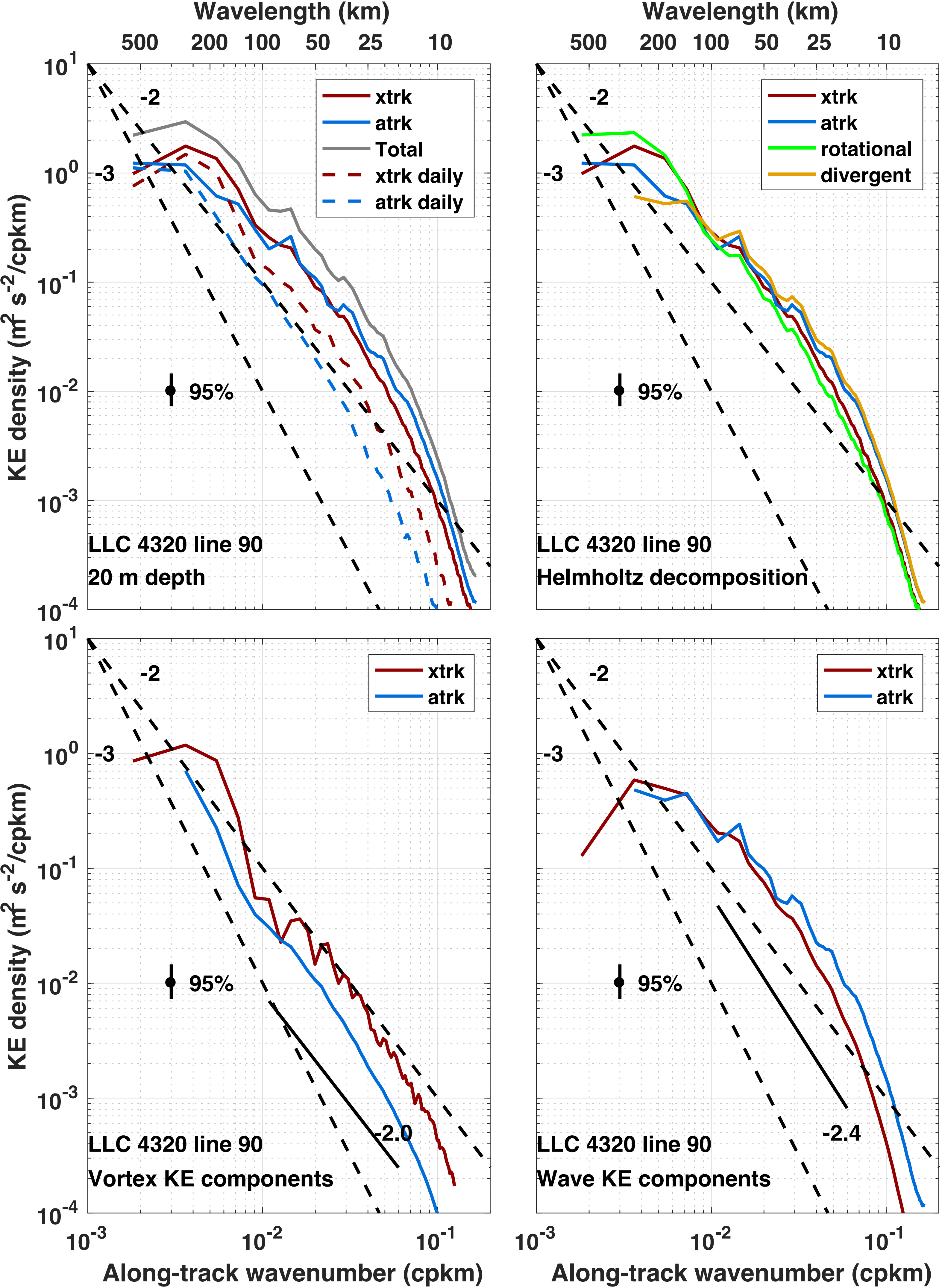
Wavelength (km)
500
200
100
50
25
10
Wavelength (km)
500
200
100
50
25
10
10^{1}
10^{0}
10^{-1}
10^{-2}
10^{-3}
10^{-4}
KE density (m^2 s^{-2}/cpkm)
-2
-3
xtrk
atrk
Total
xtrk daily
atrk daily
95%
LLC 4320 line 90
20 m depth
-2
-3
xtrk
atrk
rotational
divergent
95%
LLC 4320 line 90
Helmholtz decomposition
10^{1}
10^{0}
10^{-1}
10^{-2}
10^{-3}
10^{-4}
KE density (m^2 s^{-2}/cpkm)
-2
-3
xtrk
atrk
95%
-2.0
LLC 4320 line 90
Vortex KE components
-2
-3
xtrk
atrk
95%
-2.4
LLC 4320 line 90
Wave KE components
10^{-3}
10^{-2}
10^{-1}
Along-track wavenumber (cpkm)
10^{-3}
10^{-2}
10^{-1}
Along-track wavenumber (cpkm)

Figure 7.

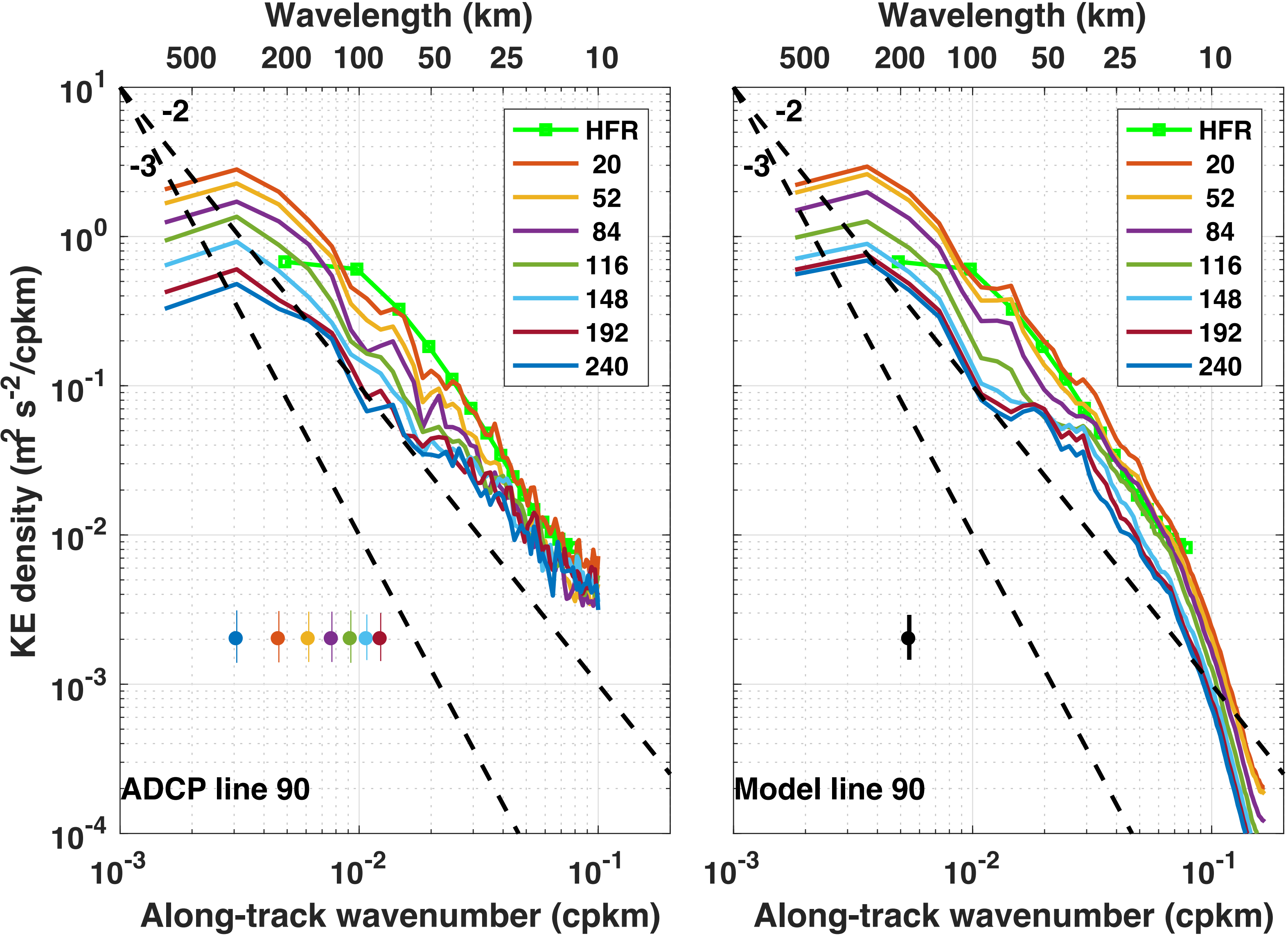
Wavelength (km)
500
200
100
50
25
10
Wavelength (km)
500
200
100
50
25
10
KE density (m^2 s^{-2}/cpkm)
10^1
10^0
10^{-1}
10^{-2}
10^{-3}
10^{-4}
-2
-3
-2
-3
HFR
20
52
84
116
148
192
240
HFR
20
52
84
116
148
192
240
ADCP line 90
Model line 90
10^{-3}
10^{-2}
10^{-1}
10^{-3}
10^{-2}
10^{-1}
Along-track wavenumber (cpkm)
Along-track wavenumber (cpkm)

Figure 8.

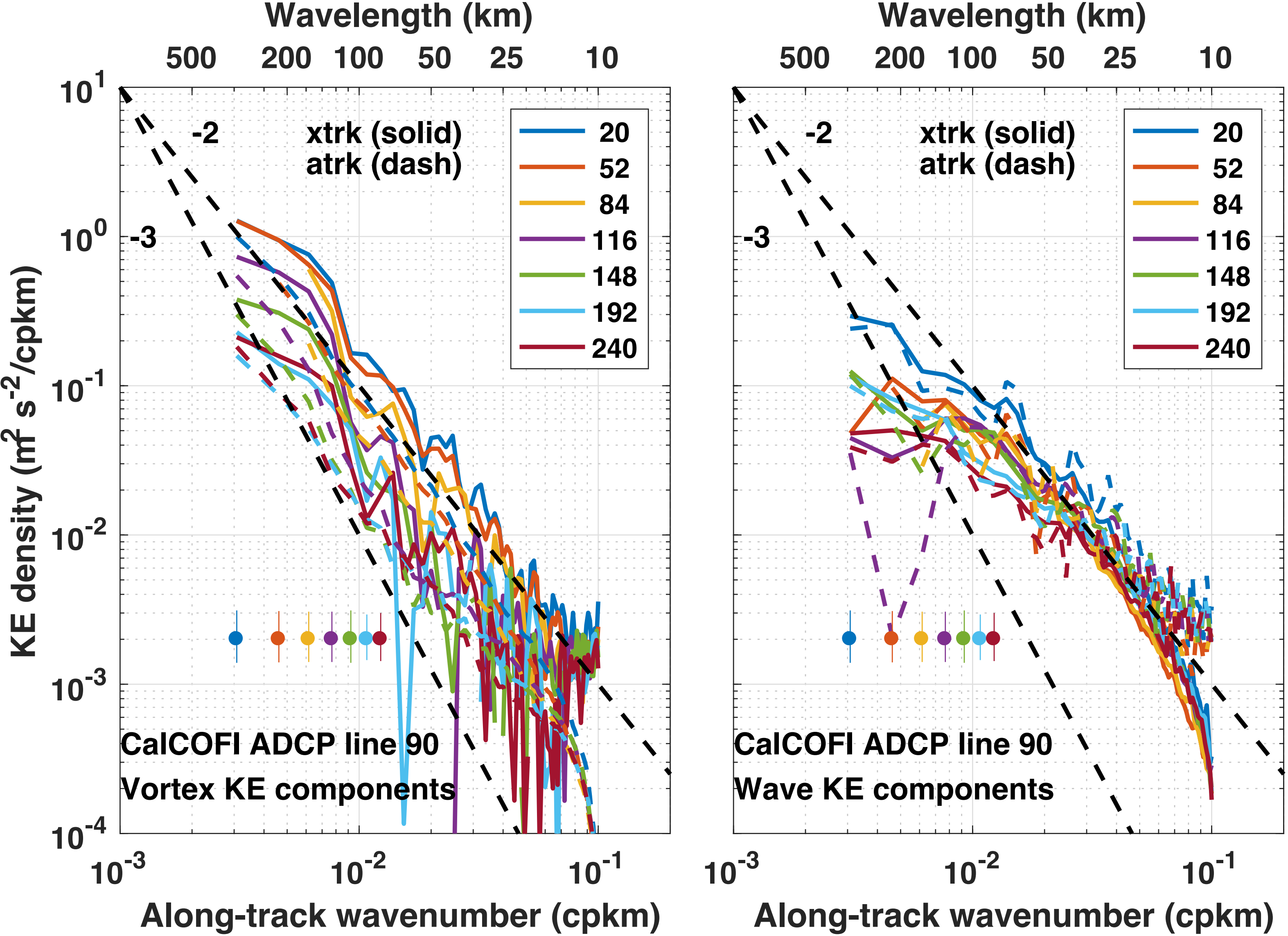
Wavelength (km)
500
200
100
50
25
10
KE density ($m^2 s^{-2}$/cpkm)
10^1
10^0
10^{-1}
10^{-2}
10^{-3}
10^{-4}
-2
-3
xtrk (solid)
atrk (dash)
20
52
84
116
148
192
240
CalCOFI ADCP line 90
Vortex KE components
Wave KE components
10^{-3}
10^{-2}
10^{-1}
Along-track wavenumber (cpkm)

Figure 9.

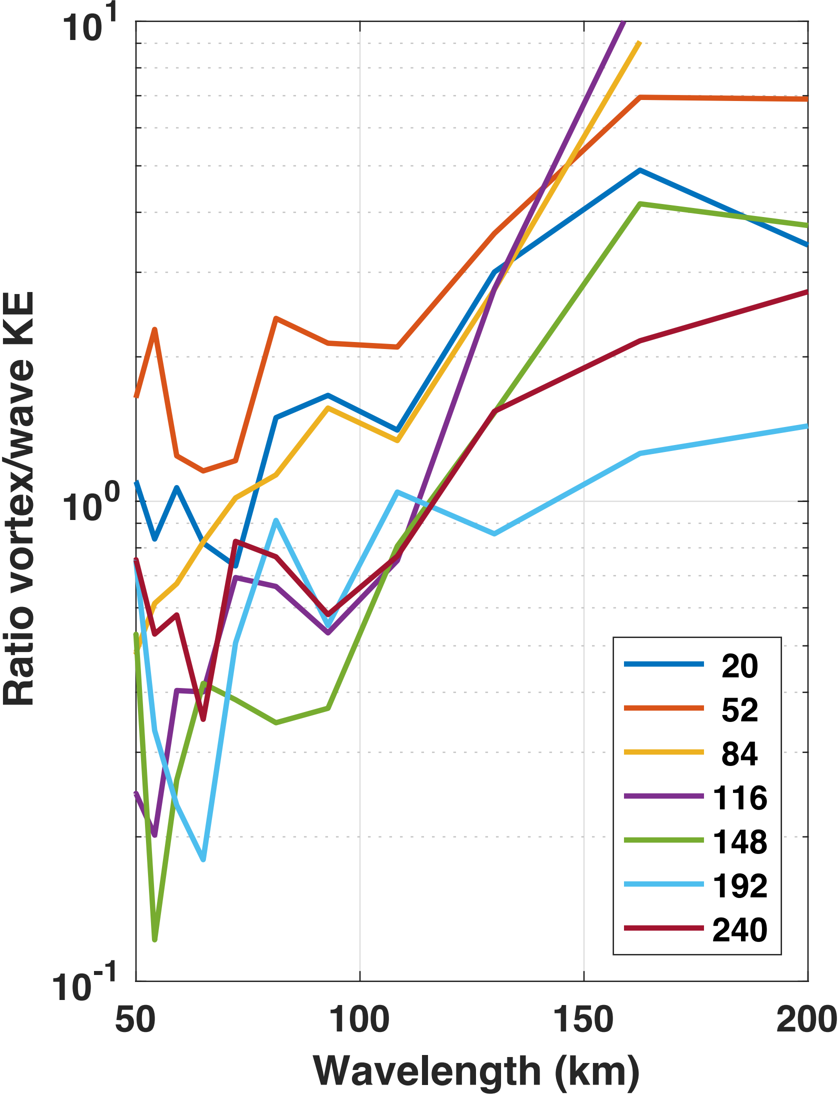

10^1
10^0
10^{-1}
Ratio vortex/wave KE
50
100
150
200
Wavelength (km)
20
52
84
116
148
192
240

Figure 10.

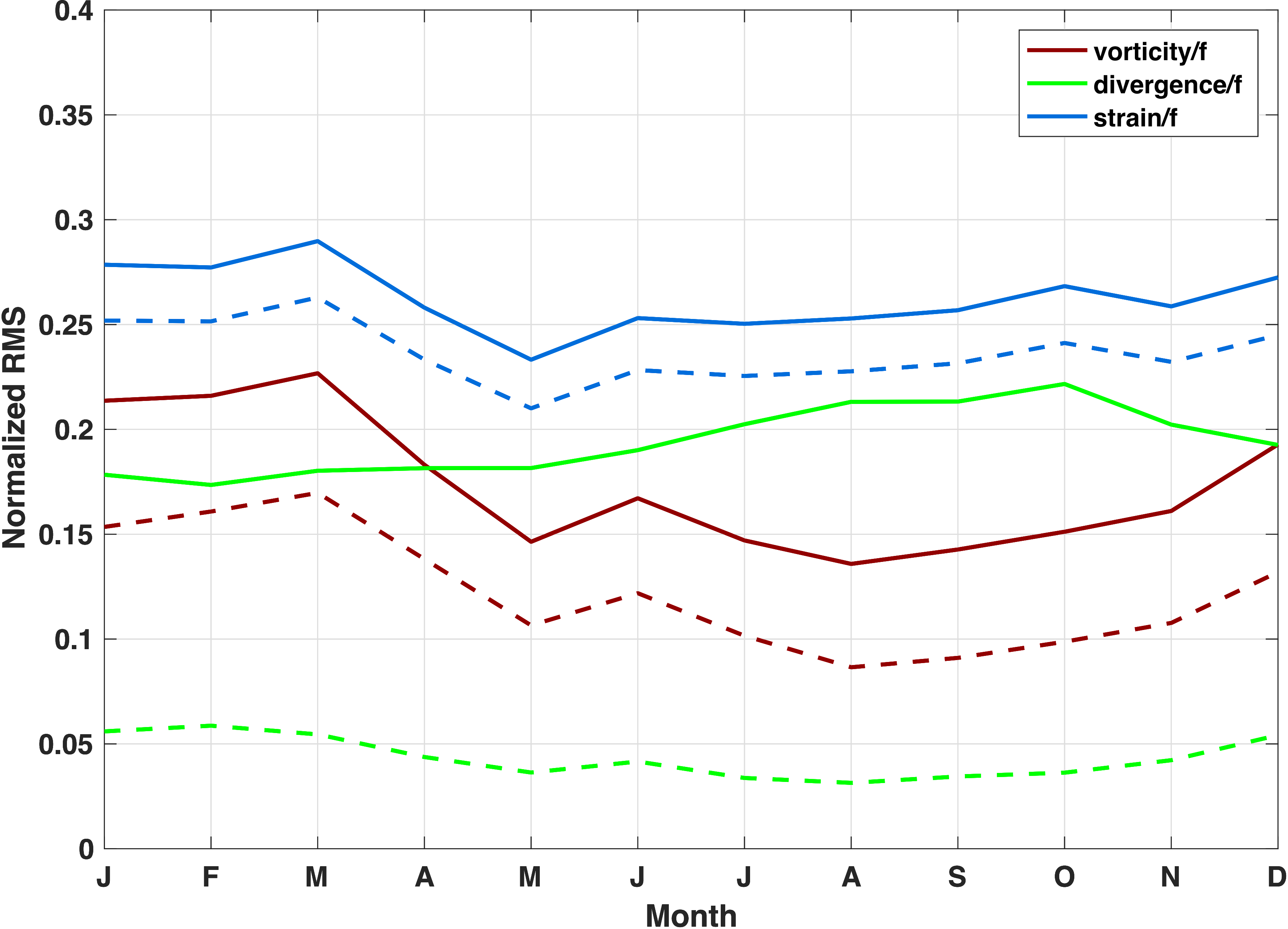
0.4
0.35
0.3
0.25
0.2
0.15
0.1
0.05
0
Normalized RMS
J
F
M
A
M
J
J
A
S
O
N
D
Month
vorticity/f
divergence/f
strain/f

Figure 11.

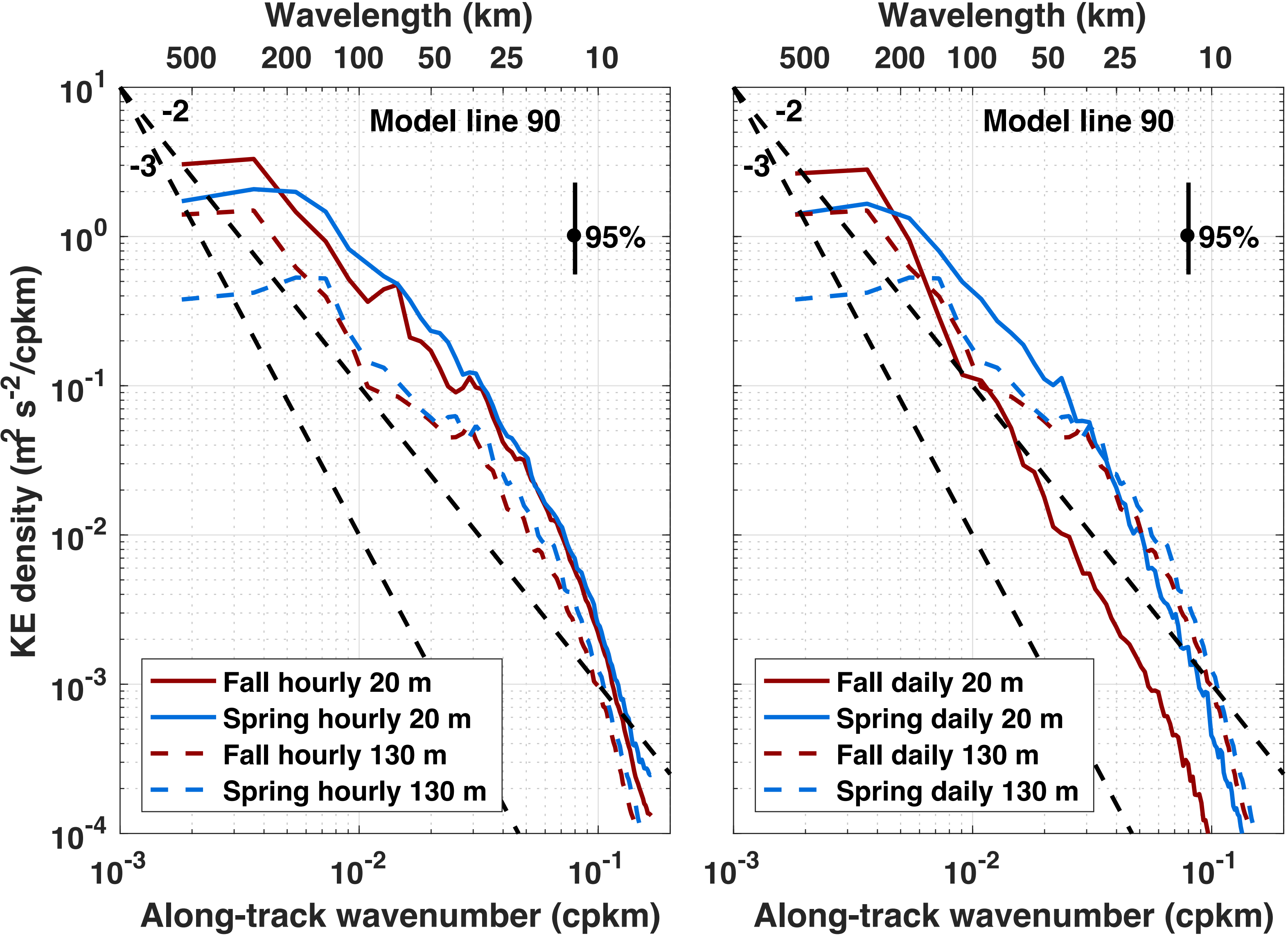
Wavelength (km)
500
200
100
50
25
10
Model line 90
-2
-3
95%
KE density (m^2 s^{-2}/cpkm)
10^{1}
10^{0}
10^{-1}
10^{-2}
10^{-3}
10^{-4}
Fall hourly 20 m
Spring hourly 20 m
Fall hourly 130 m
Spring hourly 130 m
10^{-3}
10^{-2}
10^{-1}
Along-track wavenumber (cpkm)
Wavelength (km)
500
200
100
50
25
10
Model line 90
-2
-3
95%
Fall daily 20 m
Spring daily 20 m
Fall daily 130 m
Spring daily 130 m
10^{-3}
10^{-2}
10^{-1}
Along-track wavenumber (cpkm)

Figure 12.

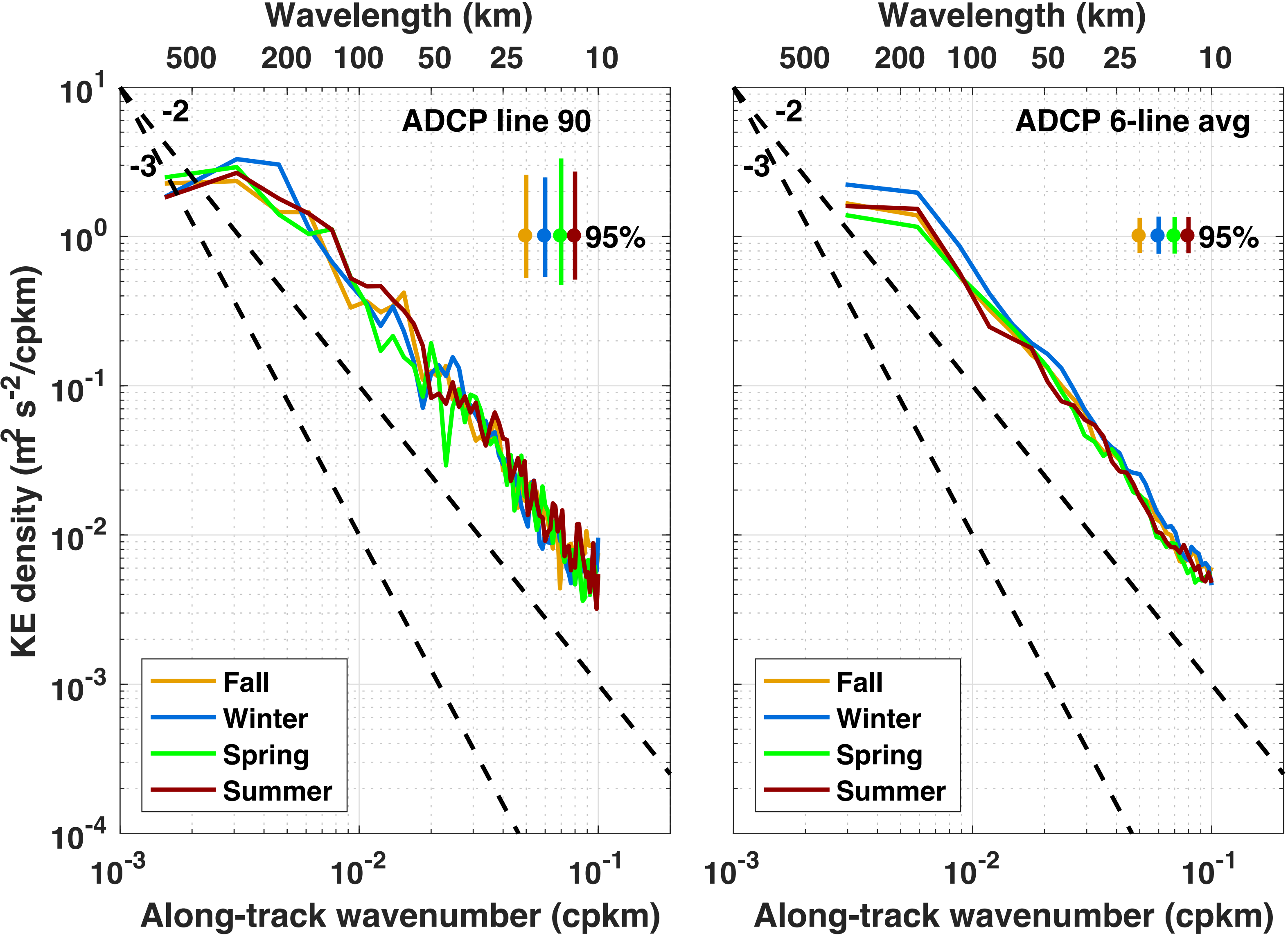
Wavelength (km)
500
200
100
50
25
10
ADCP line 90
-2
-3
95%
Fall
Winter
Spring
Summer
KE density (m^2 s^{-2}/cpkm)
10^1
10^0
10^{-1}
10^{-2}
10^{-3}
10^{-4}
10^{-3}
10^{-2}
10^{-1}
Along-track wavenumber (cpkm)
Wavelength (km)
500
200
100
50
25
10
ADCP 6-line avg
-2
-3
95%
Fall
Winter
Spring
Summer
10^{-3}
10^{-2}
10^{-1}
Along-track wavenumber (cpkm)

Figure 13.

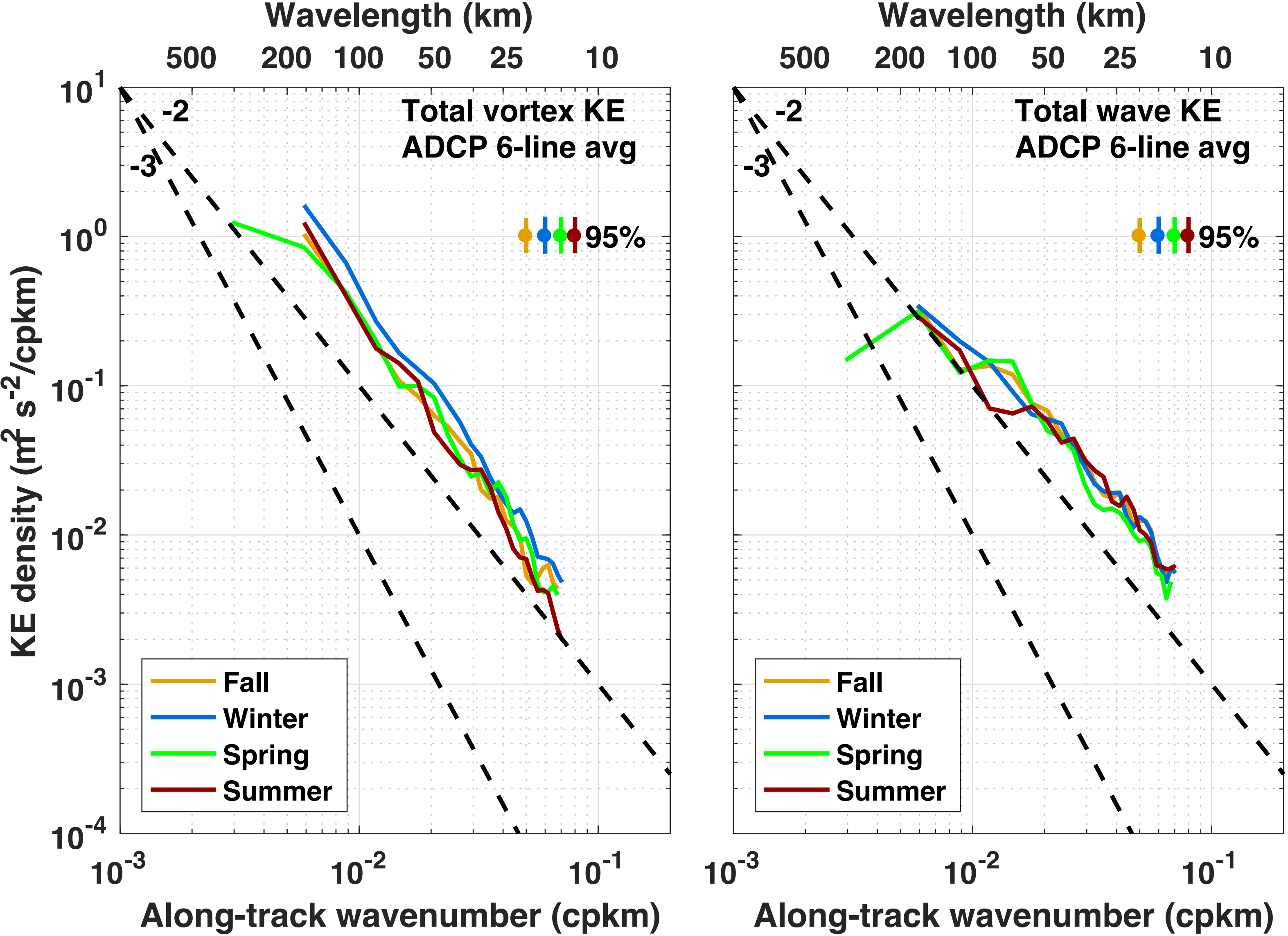
Wavelength (km)
500
200
100
50
25
10
Total vortex KE
ADCP 6-line avg
-2
-3
95%
KE density (m^2 s^{-2}/cpkm)
10^1
10^0
10^{-1}
10^{-2}
10^{-3}
10^{-4}
Fall
Winter
Spring
Summer
10^{-3}
10^{-2}
10^{-1}
Along-track wavenumber (cpkm)
Wavelength (km)
500
200
100
50
25
10
Total wave KE
ADCP 6-line avg
-2
-3
95%
Fall
Winter
Spring
Summer
10^{-3}
10^{-2}
10^{-1}
Along-track wavenumber (cpkm)

Figure 14.

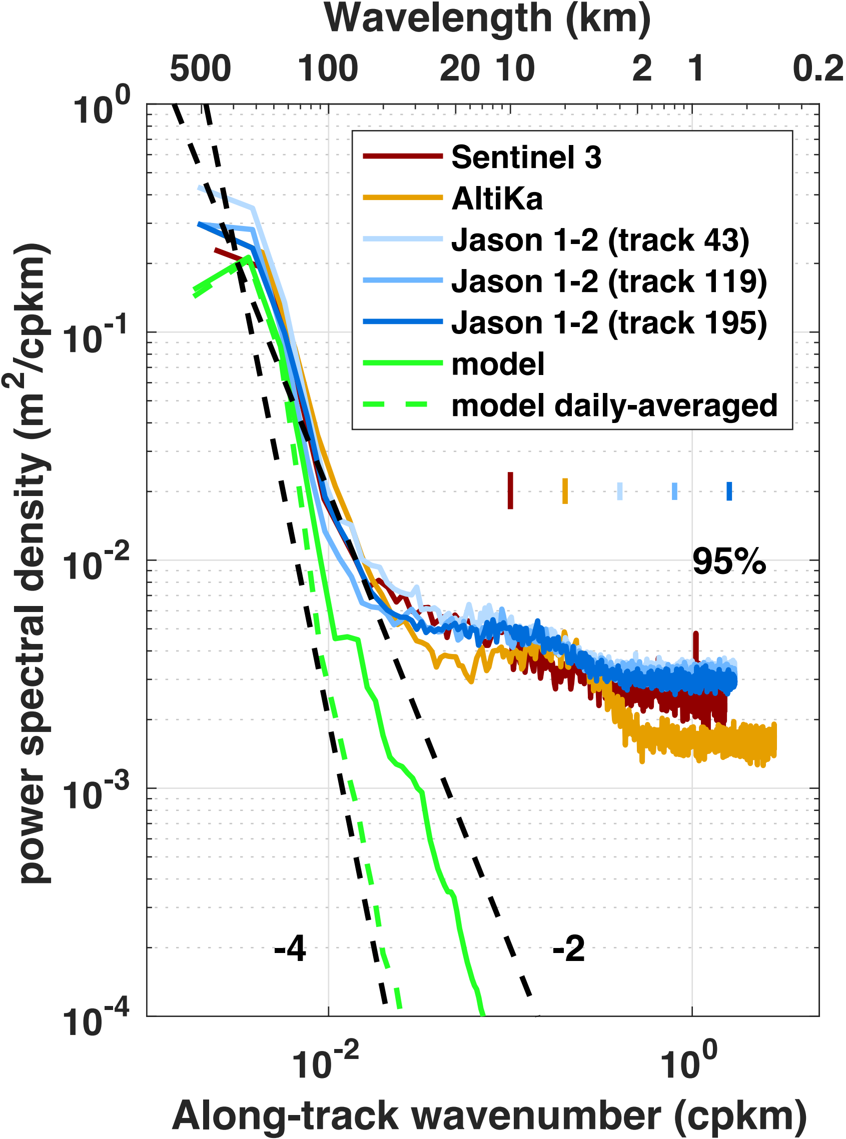
Wavelength (km)
500
100
20
10
2
1
0.2
10^0
10^{-1}
10^{-2}
10^{-3}
10^{-4}
power spectral density (m^2/cpkm)
Sentinel 3
AltiKa
Jason 1-2 (track 43)
Jason 1-2 (track 119)
Jason 1-2 (track 195)
model
model daily-averaged
95%
-4
-2
10^{-2}
10^0
Along-track wavenumber (cpkm)

Figure 15.

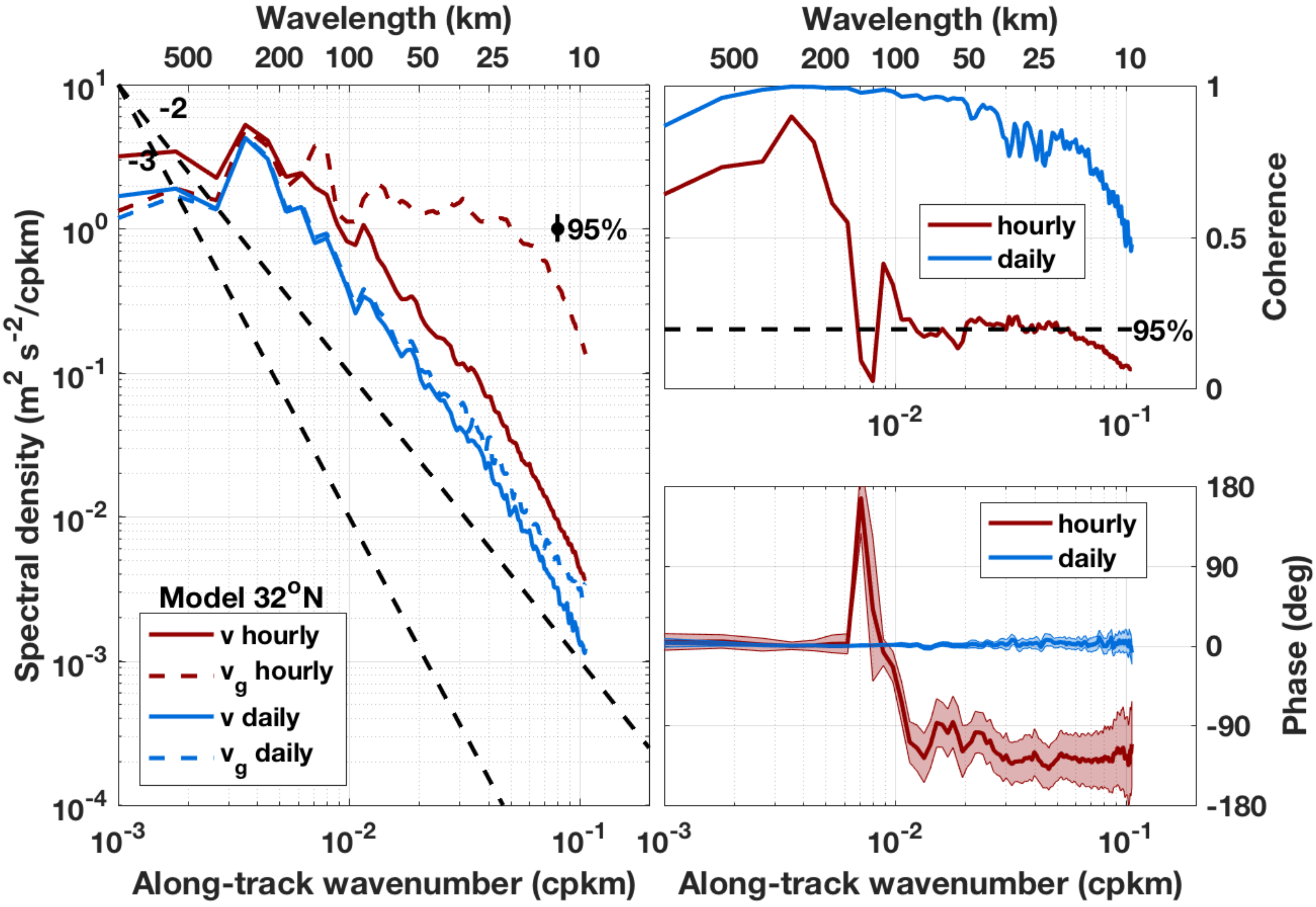
Wavelength (km)
500
200
100
50
25
10
Spectral density (m^2 s^{-2}/cpkm)
10^1
10^0
10^{-1}
10^{-2}
10^{-3}
10^{-4}
-2
-3
95%
Model 32^{o}N
v hourly
v$_g$ hourly
v daily
v$_g$ daily
10^{-3}
10^{-2}
10^{-1}
Along-track wavenumber (cpkm)
Wavelength (km)
500
200
100
50
25
10
Coherence
1
0.5
0
hourly
daily
95%
10^{-2}
10^{-1}
Phase (deg)
180
90
0
-90
-180
hourly
daily
10^{-3}
10^{-2}
10^{-1}
Along-track wavenumber (cpkm)